



Influence of the zeolite surface properties and potassium modification on the Zn-catalyzed CO₂-assisted oxidative dehydrogenation of ethane

Jiaxu Liu ^{a,*¹}, Zhenmei Zhang ^{a,1}, Yulin Jiang ^a, Xiao Jiang ^{b,*}, Ning He ^a, Siyang Yan ^a, Peng Guo ^c, Guang Xiong ^a, Ji Su ^d, Gianvito Vilé ^e

^a State Key Laboratory of Fine Chemicals & Department of Catalytic Chemistry and Engineering, Dalian University of Technology, Dalian 116024, China

^b Aramco Americas: Aramco Research Center - Boston, 400 Technology Square, Boston, MA 02139, USA

^c State Key Laboratory of Heavy Oil Processing, China University of Petroleum (East China), Qingdao 266580, China

^d Materials Sciences Division, Molecular Foundry, Material Science Division, Lawrence Berkeley National Laboratory, Berkeley, CA 94720, USA

^e Department of Chemistry, Materials and Chemical Engineering "Giulio Natta", Politecnico di Milano, Piazza Leonardo da Vinci 32, 20133 Milano, Italy

ARTICLE INFO

Keywords:

CHA zeolite
Zinc nanoparticles
Potassium modification
Ethylene
Oxidative dehydrogenation

ABSTRACT

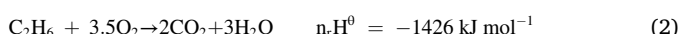
Zeolites with incorporated Zn species are gaining relevance for catalyzing the dehydrogenation of short-chain alkanes. However, the presence of zinc also leads to the C-C cleavage in the alkane, lowering the selectivity to the olefin. We disclose herein the importance of controlling the zeolite particle size and the promoting role of K₂O addition to improve the alkene selectivity and catalyst stability during Zn-catalyzed CO₂-assisted oxidative dehydrogenation of ethane. In particular, the nano-sized SSZ-13 catalysts outperform the micro-sized SSZ-13 catalysts in terms of C₂H₆ conversion due to the critical role of zeolite crystal surface properties that improves the dispersion of the Zn phase. The modification of Zn with K₂O neutralizes the acidity of the catalysts, suppressing the formation of undesired paths and leading to higher C₂H₄ selectivity and improved stability. Detailed characterizations and density functional theory show that K₂O-neighbored (Zn-O-Zn)²⁺ lowers the activation barrier for the surface removal of H-based adsorbates. Overall, these findings demonstrate the roles of fine-tuning acid-base properties on the zeolite surface to control the catalytic performance during the CO₂-assisted conversion of light alkanes.

1. Introduction

Ethylene (C₂H₄) is a central organic feedstock for a large number of chemicals, being employed to manufacture styrene, ethylene oxide, vinyl chloride, vinyl acetate monomers, functional hydrocarbons (*i.e.*, dichloroethane, ethylbenzene, acetaldehyde, and ethanol), polymers, and other basic and intermediate products [1]. Ethylene is conventionally produced from naphtha and gasoil *via* steam cracking. However, the recent rise in shale gas production and the availability of large shale gas reserves have substantially changed the ethylene production landscape [2]. Shale gas is, in fact, an abundant and accessible resource, and each of its components can be utilized directly or serve as a precursor to form value-added chemicals and fuels. Depending on the source of shale gas, up to 15 vol% of it is composed of light alkanes, such as C₂H₆, C₃H₈, and C₄H₁₀, with C₂H₆ being the most abundant component [3]. Hence, the production of ethylene from shale-gas derived ethane is revitalizing

the chemical industry.

Although steam cracking has been applied for decades, this reaction suffers from short lifecycles, low conversion and selectivity, as well as from the inherent thermodynamic limit at high temperatures [4]. Oxygen-assisted oxidative dehydrogenation of ethane (O₂-ODHE) provides a solution to some of these issues [5], and it can be applied to the production of ethylene from shale-gas derived ethane. The reaction consists of the selective oxidation of ethane to ethylene at 100 °C as a main reaction (Eq. 1) and the over-oxidation of ethane and ethylene as side reactions (Eqs. 2–5):

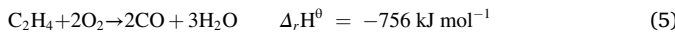
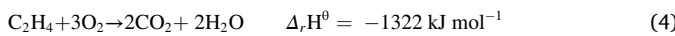


* Corresponding authors.

E-mail addresses: liujiayu@dlut.edu.cn (J. Liu), xiao.jiang@aramcoamericas.com (X. Jiang), gianvito.vile@polimi.it (G. Vilé).

¹ Contributed equally.





However, the strong oxidative potential of oxygen leads to over-oxidation to the undesired carbon oxides (CO_x), therefore reducing the selectivity toward the alkene [6,7]. As shown in the recent work of Deshlahra and Iglesia [8], the C-H activation selectivity can be correlated with the strength of the H abstractor and the strength of the C-H bond. Ethane to ethylene, particularly, is a partial oxidation in which the C-H bonds of the product (ethylene) are stronger than those of the reactant (ethane). Based on this work, recent efforts have focused on substituting the O_2 with soft oxidants, such as CO_2 [9], N_2O [6,10], and SO_2 [11]. Among those, a unique advantage of using CO_2 is to improve the stability by inhibiting coking during CO_2 -ODHE via the reverse Boudouard reaction ($\text{C} + \text{CO}_2 \rightarrow 2\text{CO}$) [12]. Besides, the utilization of CO_2 in catalysis is envisioned as a necessity, as it could not only enable the full utilization of carbon resource, but also help to alleviate CO_2 emissions via a hydrogen-free and environmentally-friendly approach to produce value-added chemicals and fuels [13–15]. Hence, the possibility to convert C_2H_6 to C_2H_4 in the presence of CO_2 is an attractive and technically-viable approach [16,17].

To date, various support materials have been employed to prepare the catalysts for ODHE, including metal oxides such as SiO_2 , ZrO_2 , Al_2O_3 , and TiO_2 , as well as porous inorganic materials such as TS-1 (MFI framework), ZSM-5 (MFI framework), clinoptilolite, and SAPO-34 (CHA framework) [18–22]. Zeolites are particularly attractive, as they feature tridimensional, microporous structure, large specific surface area, tunable acidity, and good hydrothermal and mechanical stability [23]. SSZ-13 (CHA framework) is microporous silica-aluminate with a tetrahedral framework and composed of a layer of double 6-membered rings with a sequence of ABCABC and CHA cavities connected to the six neighboring cages by 8-membered rings, the sorption aperture of which is *ca.* 3.8 nm in width [24]. This material also exhibits excellent CO_2 adsorption capacity at ambient conditions [25,26]. Reactant-shape selectivity is another important feature of zeolite-based catalysts [27], rendering them applicable in petrochemical processes, such as ZSM-5 with 3D channels for selective production of C_5^+ hydrocarbons (*i.e.*, aromatics and alkanes) [28–30].

The modification of silica, ZSM-5, and Beta zeolite with Zn ions has attracted great attention due to their outstanding performance in promoting the dehydrogenation of short-chain alkanes [31–36]. Our recent work has reported that micro-sized SSZ-13 with incorporated $(\text{Zn}-\text{O}-\text{Zn})^{2+}$ active species exhibits high catalytic performance in CO_2 -ODHE [37]. We have shown that $(\text{Zn}-\text{O}-\text{Zn})^{2+}$ active species over HZSM-5 are effective in activating C-H bond of short-chain alkanes at low temperatures. However, the presence of these species is also effective in cleaving the C-C bond, inevitably lowering the selectivity to the target C_2H_4 and producing undesired CH_4 [38–41]. Clearly, such a contrast brings the necessity to properly modify the zeolite active sites, and this is typically done by modifying the metal phase [41]. In this work, we propose to tune the zeolite particle size and introduce an alkali metal oxide, K_2O , into Zn-based SSZ-13 catalysts to suppress the C-C bond cleavage by effectively tuning the zeolite acid-base properties. Therefore, we present bimetallic (*i.e.*, K and Zn) nano-sized SSZ-13 zeolite materials as novel catalysts for CO_2 -ODHE, which not only exhibit higher conversions of both C_2H_6 and CO_2 but also present well-retained C_2H_4 selectivity and stability. The structure-reactivity relationships have been elucidated based on a combination of experimental and theoretical studies.

2. Experimental

2.1. Catalyst preparation

Micro-sized H-SSZ-13 zeolite (with a Si/Al molar ratio of 20 and

particles of *ca.* 1–3 μm , hereafter denoted as HS-U), micro-sized H-SSZ-13 zeolite (with a Si/Al molar ratio of 14 and particles of *ca.* 1–3 μm , hereafter denoted as HS-U14), and nano-sized H-SSZ-13 zeolite (with a Si/Al molar ratio of 14 and particles of *ca.* 20–50 nm, hereafter denoted as HS-N) were all purchased by Dalian Ligong Qiwangda Chemical Technology (Dalian, China). All chemicals were analytical grade and were used as such, without further purification or modification. Sodium nitrate (NaNO_3 , 99.9%), zinc acetate ($\text{Zn}(\text{CH}_3\text{COO})_2 \cdot 2\text{H}_2\text{O}$, 99.9%), and potassium nitrate ($\text{KNO}_3 \cdot 9\text{H}_2\text{O}$, 99.9%) were purchased from Sinopac Chemical Reagent Co. LTD and also used as such.

The micro and nano-sized NaSSZ-13 zeolites (hereafter denoted as NaS-U and NaS-N, respectively) were prepared by exchanging for 2 h the parent HS-U and HS-N materials four times at 80 °C, using a 1 M solution of NaNO_3 and at a liquid-to-solid weight ratio of 5. The samples were filtered and washed with deionized water after each exchange, dried at 110 °C for 12 h, and finally calcined at 650 °C in dry air for 3 h. The Zn-modified micro and nano-sized NaSSZ-13 zeolites, namely respective $\text{Zn}_x/\text{NaS-U}$ and $\text{Zn}_x/\text{NaS-N}$, were prepared by incipient wetness impregnation using a 1 M $\text{Zn}(\text{CH}_3\text{COO})_2$ solution as the precursor. The IWI was carried out at 80 °C for 2 h. The impregnated samples were then dried at 110 °C for 12 h prior to calcination at 650 °C for 3 h.

The bimetallic $\text{Zn}_x\text{K}_y/\text{NaS-N}$ catalysts were prepared by loading Zn and subsequently K onto the as-prepared NaSSZ-13 *via* IWI, wherein x and y indicate the weight percentage of Zn and K, respectively. The impregnation of K on the Zn/NaS-N was carried out in an aqueous 1 M solution of $\text{K}(\text{NO}_3)_3 \cdot 9\text{H}_2\text{O}$ at 80 °C for 4 h. The impregnated samples were dried at 110 °C for 12 h, and then calcined at 650 °C for 6 h to obtain the $\text{Zn}_x\text{K}_y/\text{NaS-N}$ catalyst. Table S1 reports the compositional analysis of the samples. The amount of metals was chosen to be close to the nominal values of 2, 4, 6, and 8 wt% (for Zn), and 0.7, 1.4, and 2.1 wt% (for K). By *systematically* selecting increasing values of Zn and K, we aimed at addressing the effect of metal content on the catalysis.

2.2. Characterizations

X-ray diffraction (XRD) patterns were recorded by a Rigaku D/max-2004 diffractometer with $\text{Cu K}\alpha$ radiation (40 kV, 100 mA) at a 2° min^{-1} scanning speed and in the 2θ range between 5° and 60°. X-ray fluorescence (XRF) measurements were performed with a Bruker SRS3400 spectrometer to determine the silicon to aluminum ratio as well as the Zn and K weight percentage. Nitrogen physisorption was performed on a Micromeritics ASAP 3020 instrument at –196 °C to obtain textural information. Prior to the measurement, the samples (380–830 μm sieve fraction) were degassed at 340 °C for 5 h. The surface area was calculated by the Brunauer-Emmett-Teller (BET) method using the adsorption branch in the p/p_0 range from 0.10 to 0.15, and the pore volumes were estimated at p/p_0 of 0.99, while the micro- and mesoporous were discriminated by the *t*-plot method. Temperature-programmed desorption of ammonia (NH_3 -TPD) was employed to investigate the strength of the acid sites in the catalysts. The profiles were obtained on a Quantachrome ChemBet 3000 chemisorb instrument. The samples (*ca.* 150 mg, 380–830 μm sieve fraction) were pretreated in He (99 wt% purity, Dalian Special Gases Co. LTD) at 600 °C for 1 h and then cooled down to 100 °C for ammonia adsorption studies. The ammonia (99 wt% purity, Dalian Special Gases Co. LTD) adsorption was carried out at 100 °C for 30 min with a mixture of 5 vol% NH_3/He . After adsorption, the cell was purged with 50 mL min^{-1} He for 30 min to remove the non-chemisorbed NH_3 . Then, the NH_3 -TPD profiles were recorded in a 50 mL min^{-1} He flow by ramping the temperature from 100 °C to 600 °C at a rate of *ca.* 16 °C min^{-1} . Temperature-programmed reduction in H_2 (H_2 -TPR) was conducted on a Quantachrome ChemBET Pulsar Chemisorption instrument. Prior to the analysis, the samples (0.15 g) were pretreated in helium at 450 °C for 1 h. Afterward, the powders were cooled to 50 °C in He. Finally, temperature-programmed reduction was carried out in a flow of H_2/Ar mixture (120 mL min^{-1} , 10% H_2), ranging the temperature from 100 °C to 800 °C at a heating rate of

10 °C min⁻¹. Temperature-programmed desorption of carbon dioxide (CO₂-TPD) was conducted by using the same instrument above. In particular, the samples (0.15 g) were pretreated in helium at 450 °C for 1 h. Then, the materials were cooled down to 50 °C in He. CO₂-TPD was conducted by heating the samples from room temperature to 450 °C at a rate of 10 °C min⁻¹ in 5 vol% CO₂/N₂ (120 mL min⁻¹). High-resolution transmission electron microscopy (HRTEM) and high-angle annular dark field scanning transmission electron microscopy (HAADF-STEM) images were acquired on a FEI (Tecnai F30 G2, The Netherlands) microscopy. Scanning electron microscopy (SEM) images were collected on a Hitachi S-4800 microscope. Thermogravimetric analysis (TGA) of the materials was studied on the STA 449 F3 thermogravimetric analyzer coupled with a QMS 403D mass spectrometer (NETZSCH, Germany). The analysis mode was DTA-TGA. For each measurement, *ca.* 11 mg of catalyst were placed in an alumina crucible, followed by ramping the temperature from room temperature to 900 °C at 10 °C min⁻¹ in a flowing (50 mL min⁻¹) air atmosphere. The amount of carbon deposit in the used catalysts was calculated according to the weight loss in the temperature range from 400° to 700°C. UV-Vis diffuse reflectance spectra (UV-Vis-DRS) were collected at 200–800 nm using BaSO₄ as a reference on an Agilent Cary 5000 UV-Vis-NIR spectrophotometer with diffuse reflectance integration sphere attachment (Internal DRA 2500). Fourier-transform infrared spectroscopy (FTIR) was employed to study the surface hydroxyl (OH) groups of the catalysts. The characterization was performed using Nicolet IS50 FTIR spectrometer in the range from 4000 to 400 cm⁻¹ with an optical resolution of 4 cm⁻¹. The zeolite samples were pressed into a self-supporting thin wafer (*ca.* 16 mg) and decontaminated at 400 °C under vacuum (*i.e.*, 10⁻³ Pa) for 4 h in a quartz IR cell equipped with CaF₂ windows. After the pretreatment, the cell was cooled down to room temperature for sample measurement. To examine the evolutions in the hydroxyl regions, the spectra were processed by subtracting the background spectrum (recorded in an empty IR cell in the absence of catalyst) from the measured sample spectra. The analysis of the OH region after NH₃ treatment was performed as follows: first, NH₃ adsorption was carried out at 150 °C under NH₃ flow (using a mixture of 10 vol% NH₃/He) at the flow rate of 3 mL min⁻¹ for 30 min. Then, the sample was evacuated (10⁻³ Pa) for 30 min. The sample was then heated to 150 °C or 300 °C for analysis. The spectra were obtained by subtracting the background (obtained with decontaminated wafers before NH₃ adsorption) from the measured sample spectra. CO adsorption over Zn modified SSZ-13 zeolite sites was characterized at liquid nitrogen temperature (~196 °C) over dual beam Fourier-transform infrared spectroscopy (CO-DB-FTIR) using Nicolet IS50 FTIR spectrometer in the range from 4000 to 400 cm⁻¹ with an optical resolution of 4 cm⁻¹ [38]. The zeolite samples were pressed into a self-supporting thin wafer (*ca.* 16 mg) and decontaminated at 400 °C under vacuum (*i.e.*, 10⁻³ Pa) for 4 h in a quartz dual beam FTIR cell equipped with CaF₂ windows. After the pretreatment, the cell was cooled down to liquid nitrogen temperature, 10 mL CO (99.99% purity) were fed for 30 min (thus, using a flow rate of 0.33 mL min⁻¹), and then the cell was evacuated. The spectra were processed by subtracting the background spectrum (recorded in the reference IR cell in the absence of catalyst) from the measured sample spectra. X-ray photoelectron spectroscopy (XPS) were performed using the monochromatic Al K α X-rays source and the achromatic Mg K α /Al K α dual anode X-ray source. The monochromatic Al K α anode (1486.6 eV) was used at 150 W and 15 kV. XPS spectra were recorded at 90° takeoff angle from the surface of the sample holder using the aperture slot of 300 × 700 μ m.

2.3. Activity tests

A continuous fixed-bed reactor was used to evaluate the catalyst activity during CO₂-ODHE. If not specified otherwise, the catalyst was crushed and sieved into 20–40 mesh particles. Typically, *ca.* 1.0 g catalyst was loaded in a stainless-steel reactor with 600 mm length and 10 mm internal diameter. The temperature of the catalyst bed was

monitored by a thermocouple that touched the center of the bed. Prior to any activity measurement, the catalyst was pretreated at 550 °C for 1 h in Ar to remove adsorbed water. During the test, a feed mixture with C₂H₆:CO₂:Ar volume ratio of 1:1:18 was introduced into the reactor at a flow rate of 60 mL min⁻¹. The gas flows were controlled with Bronkhorst mass flow controllers. The product and unreacted substrates were analyzed by two inline gas chromatographs. One of them was equipped with a Pora Plot Q capillary column and a flame ionization detector for hydrocarbons analyses; the second chromatograph was equipped with a column (3 m × 3 mm) packed with Carboxen 1000 and a thermal conductivity detector for H₂, CO, and CO₂ analyses. The catalytic tests for each sample were conducted at temperatures ranging from 550° to 650°C. The samples were kept at each condition for 20 min. Only the results acquired in the isothermal zone of each step were considered valid for analysis and discussion. All data points were collected using fresh samples. Although a steady-state operation was not possible given the transient behavior of the catalyst, the systematic way in which the samples were collected makes the comparison meaningful.

The conversions of C₂H₆ and CO₂, the selectivity to C₂H₄, and the reaction rate were determined using the equations reported elsewhere [25,26,42], as follows:

$$C_2H_6 \text{ conversion (\%)} = \frac{n_{C_2H_6,\text{in}} - n_{C_2H_6,\text{out}}}{n_{C_2H_6,\text{in}}} \times 100$$

$$C_2H_4 \text{ selectivity (\%)} = \frac{n_{C_2H_4,\text{out}}}{n_{C_2H_6,\text{in}} - n_{C_2H_6,\text{out}}} \times 100$$

$$CO_2 \text{ conversion (\%)} = \frac{n_{CO_2,\text{in}} - n_{CO_2,\text{out}}}{n_{CO_2,\text{in}}} \times 100$$

$$C_2H_4 \text{ formation rate} (\mu\text{mol min}^{-1} g^{-1}) = \frac{n_{C_2H_6,\text{in}}}{m_{\text{cat}}} \times \frac{C_2H_6 \text{ conversion}}{100} \times \frac{C_2H_4 \text{ selectivity}}{100}$$

$$\text{Carbon balance (\%)} = \frac{C_{\text{in}} - C_{\text{out}}}{C_{\text{in}}} \times 100$$

wherein n_i is the molar rate of component i , m_{cat} is the catalyst mass, and C represents the total carbon content. It is important to highlight that, despite rates should be normalized to the number of active centers and not per unit mass of the catalyst, the rate was used to compare catalysts reported in the literature, and given that the amount of active sites were not always reported, it was necessary for us to use the catalyst mass.

2.4. Computational methods

The 48 T model obtained by cutting the periodic CHA-type zeolite was used (Fig. 1). The dangling bonds were saturated with hydrogen atoms pointing to the next lattice oxygen atom, and the Si—H bond length was set to 1.46 Å. The calculations were performed on the Gaussian 09 program package [43]. To improve the energetic properties and consider the effect of the entire zeolite framework on the reaction mechanism, a two-layer ONIOM model was employed [44]. The regions close to catalytic reactions were treated at high-level functional ωB97XD recently developed by Chai and Head-Gordon, along with the 6-31 +G (d,p) basis set for accuracy, which is a long-range corrected functional [45]. The regions away from the active center were treated at lower-level with the universal force field (UFF). During all calculations, the positions of the terminal SiH₃ atoms were fixed, whereas the positions of the remaining atoms and guest molecules were optimized. (Zn-O-Zn)²⁺ was used as the active center, in agreement with the literature [46]. Thus, two models with or without K₂O were selected to investigate the promoting role of potassium addition. The transition state structures were characterized by means of frequency calculations with only one imaginary frequency. The intrinsic reaction coordinate

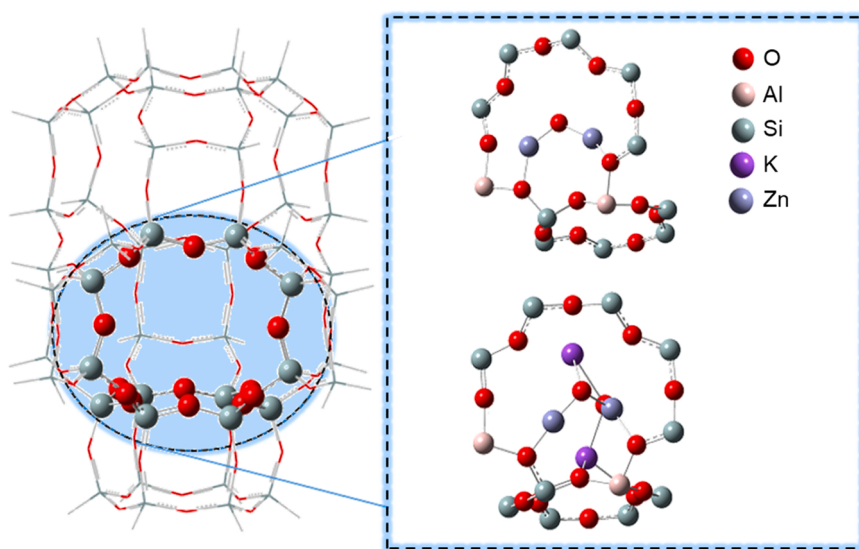


Fig. 1. Representation of the 48 T ONIOM cluster (the atoms treated with ω B97XD and UFF are depicted with ball-and-stick and with wire frame, respectively).

(IRC) method was used when it is necessary to identify the two minima connected by a transition state. To obtain accurate energies, single-point energy calculations in the optimized model were further refined at the theoretical level of ω B97XD/6-311 + +G(d, p).

3. Results and discussion

3.1. Structural characterizations

The effective incorporation of Zn and K in the sample was confirmed

by XRF. In particular, the samples are indicated with the nomenclature $Zn_xK_y/NaS-U$ and $NaS-N$, where x and y respectively indicate the Zn and K weight content measured by XRF. The XRD patterns of the micro and nano-sized SSZ-13 zeolites, before and after loading with Zn and K, are shown in Fig. S1 in the *Supplementary Data*. All samples show a characteristic chabazite (CHA) structure, featuring sharp diffraction peaks centered at 9.6° , 12.8° , 16.2° , 17.8° , 20.8° , 25.0° , 26.4° , and 31.2° [47, 48]. These diffraction peaks remain evidenced in the XRD patterns of the prepared $Zn_x/NaS-U$, $Zn_x/NaS-N$, and $Zn_xK_y/NaS-N$ catalysts, indicating the preservation of crystalline nature of the zeolite regardless of

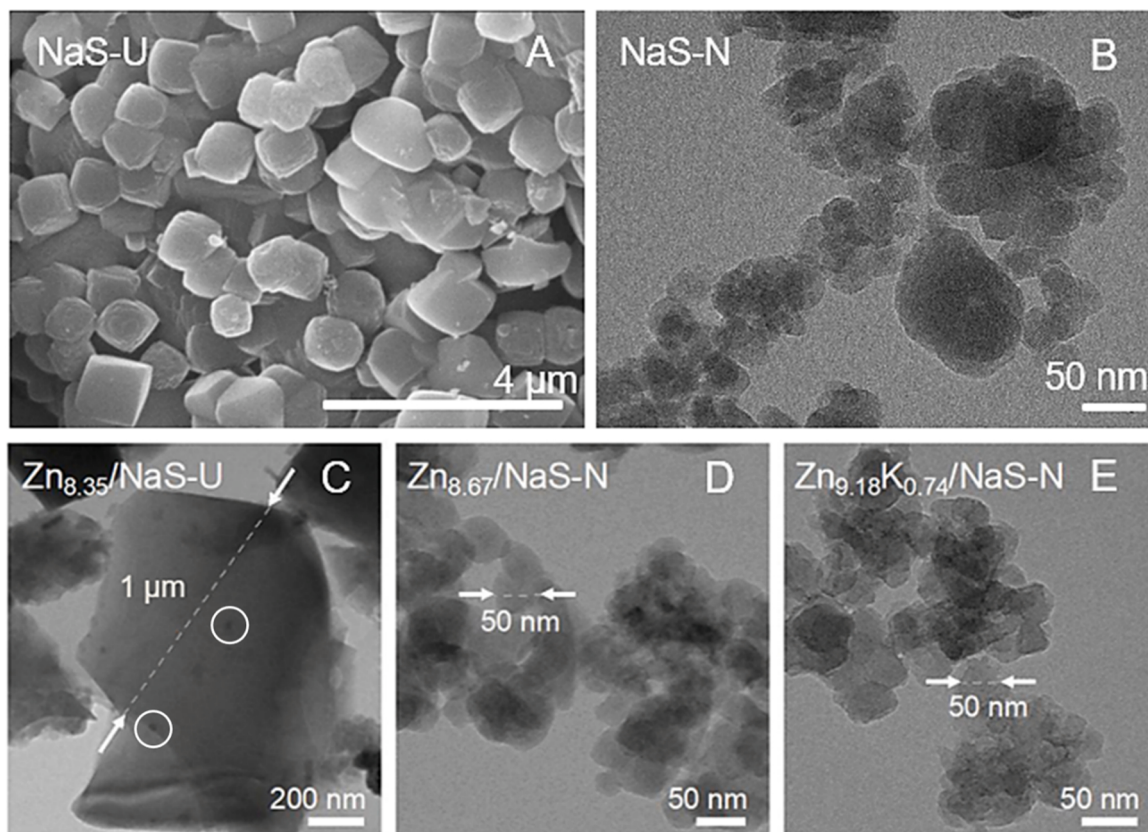


Fig. 2. SEM (A) and HRTEM (B-E) of selected micro-sized and nano-sized zeolite catalysts.

incorporating Zn or K. Notably, the peak intensities of $Zn_x/NaS\text{-}N$ and $Zn_xK_y/NaS\text{-}N$ decrease slightly with the increasing metal content, which is attributed to a reduction of the crystallite size [49]. This observation is further corroborated by microscopy. Fig. 2 shows the SEM and HRTEM images (A-B) of the micro and nano-sized SSZ-13 parent zeolites. Additional HRTEM and SEM micrographs of the parent materials are shown in Figs. S2 and S3 in the *Supplementary Data*. The micro-sized NaS-U presents highly overlapped growth and irregular zeolite crystals with an average particle size in the 1.2–1.5 μm range, while the nano-sized NaS-N displays nanoscale aggregates with 20–100 nm average particle. The same materials do not show major zinc oxide particles, pointing to the presence of a well-dispersed metal phase, which creates a uniform distribution of the active sites on the zeolite surface. Instead, over $Zn_x/NaS\text{-}U$, Zn particles with a particle of *ca.* 20 nm in diameter are observed (Fig. 2C).

Fig. 3 shows that the traditional micro-sized NaS-U exhibits a type I isotherm due to the presence of microporosity. Differently, the nano-sized NaS-N presents a characteristic type IV isotherm with an initial stage of steep uptake because of the micropores, as well as a sharp inflection at $p/p_0 = 0.8\text{--}1.0$ corresponding to the condensation within the interparticle mesopores caused by the small nanocrystals of nano-sized NaS-N. The shapes of the nitrogen adsorption-desorption isotherms show no obvious alteration upon introducing Zn and K in comparison to those of respective carriers (Fig. 3). Compared with monometallic Zn_x/NaS catalysts, the surface area and pore volume decrease with the increase of potassium addition, demonstrating that K_2O locates mainly on the external surface of the SSZ-13 zeolite (Table 1).

3.2. Acidic-basic properties

Acidic-base properties can influence the catalytic activity of zeolitic materials in hydrocarbon conversion. For this reason, Fig. 4A shows the FTIR spectra of the catalysts in the hydroxyl region. For both HS-U and HS-N parent catalyst prior to ion exchange with $NaNO_3$, the bands at 3733 and 3705 cm^{-1} correspond to the silanol groups located at the external surface and inside the micropores, respectively [50]. The broad peak at approximately 3500 cm^{-1} is attributed to the silanol nests that consist of silanol groups interacting through extended hydrogen bonding [51]. This is due to the spatial effect of the zeolitic internal defects, as well as the length and shape (chain or ring) effects of the H-bonded silanol chains in the defects. After Na modification, the bridging OH groups at 3610 cm^{-1} and 3664 cm^{-1} disappear, indicating that the H^+ from the Brønsted acid site is exchanged by Na^+ ; meanwhile, a new peak at 3633 cm^{-1} , likely attributed to weak Brønsted acid (*vide*

infra), emerges and becomes intense [52,53]. These peaks remain present upon Zn and K incorporation.

The NH_3 -TPD profiles for NaS-U, NaS-N, Zn_x -, and Zn_xK_y -containing catalysts are shown in Fig. 4B and C and provide additional insights into the acid sites. All catalysts present a major NH_3 desorption peak ranging from 150° to 350°C [54,55]. The high-temperature NH_3 desorption peak at *ca.* 450–550 °C, which appears only over the NaS-N sample, results from the interference with water due to the dehydroxylation at high temperatures [49]. Of note, the intensity of this peak in the NaS-N-based samples is slightly higher than in the NaS-U-based ones, suggesting more Lewis acid sites on NaS-N-based catalysts (see also the integrated values in Table 1). This observation is reasonable because of the higher aluminum content in NaS-N. With the loading of Zn, the total amount of acid sites increases for both NaS-U and NaS-N, which can be associated with the presence of $(Zn\text{-}O}\text{-}Zn)^{2+}$ Lewis acid sites [38]. Instead, potassium seems to decrease the amount of acid sites, as evidenced by the tail reduction around 200–300 °C. Pyridine adsorption spectroscopy is typically used to better discern between Lewis and Brønsted acid sites. However, the experiment is not possible in this case: the Van der Waals diameter of pyridine is 0.55 nm, but the micropore diameter of our SSZ-13 zeolite is only 0.38 nm. Therefore, pyridine molecules cannot diffuse through SSZ-13 channels and would only interact with the external surface of the zeolite crystallites, as shown also elsewhere [56]. To clearly differentiate Brønsted and Lewis acid sites in our samples, NH_3 -IR was applied to characterize the Lewis and Brønsted acid sites (Fig. S4). The adsorbed species at 1620 cm^{-1} over the Zn-containing SSZ-13 samples is assigned to NH_3 molecules on Lewis acid sites. The adsorbed species at 1449 cm^{-1} over the Zn-containing SSZ-13 samples is assigned to NH_3 molecules on Brønsted acid sites. The $Zn_{8.35}/NaS\text{-}U$ and $Zn_{8.67}/NaS\text{-}N$ samples obtain both Lewis and Brønsted acid sites. As the desorption temperature increases to 300 °C, the adsorbed species at 1449 cm^{-1} disappeared suggesting a weak acid strength of these Brønsted acid sites. We could also find out that the K incorporation of $Zn_{8.67}/NaS\text{-}N$ decreased the Lewis and Brønsted acidity, which indicates that the peak at 3633 cm^{-1} can be attributed to weak Brønsted acid. The NH_3 -IR results are in well accordance with the NH_3 -TPD results.

The basicity of the same catalysts was studied by CO_2 -TPD, and the resulting profiles are shown in Fig. 4D and E. A broad asymmetric CO_2 desorption peak at *ca.* 100–200 °C is observed for all catalysts, demonstrating the presence of basic sites. A Zn-induced enhancement in CO_2 adsorption is evident on both NaS-U- and NaS-N-based catalysts. In fact, adding Zn widens the temperature range of the desorption peak, indicating an increased availability of surface basic sites for CO_2 adsorption. As a result, the CO_2 adsorption capacity of $Zn_{8.67}/NaS\text{-}N$ is significantly

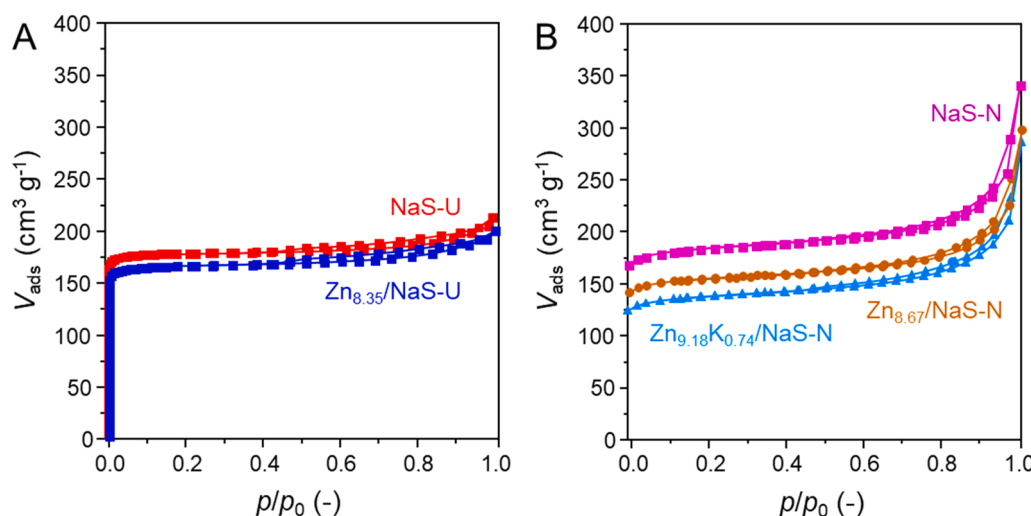
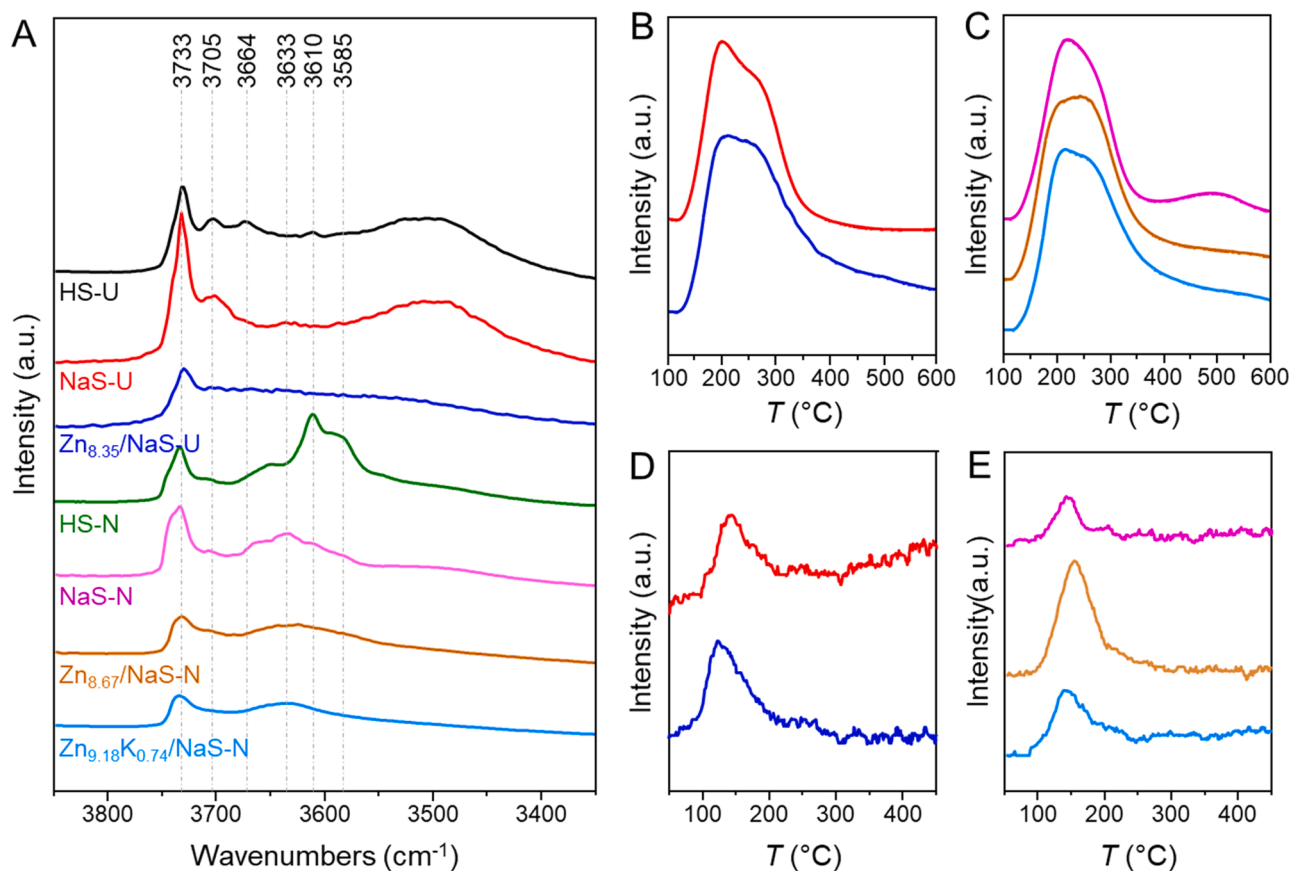


Fig. 3. N_2 adsorption-desorption isotherms of selected micro-sized (A) and nano-sized (B) zeolite catalysts.

Table 1

Textural properties and concentration of acid and basic sites for selected micro-sized and nano-sized zeolite catalysts.

Catalyst	Surface area (m^2/g)		Pore volume (cm^3/g)			Acid sites ^d (mmol/g)	Basic sites ^e (mmol/g)	Acid-to-basic site ratio (-)	Carbon deposit ^f (mg/g)
	BET ^a	Micro ^b	Total	Micro	Meso ^c				
NaS-U	632	613	0.32	0.27	0.05	0.18	0.20	70	–
Zn _{8.35} /NaS-U	562	542	0.29	0.23	0.06	0.22	0.33	51	19
NaS-N	658	589	0.49	0.25	0.24	0.20	0.20	77	–
Zn _{8.67} /NaS-N	565	541	0.40	0.21	0.19	0.23	0.80	22	38
Zn _{0.18} K _{0.74} /NaS-N	537	470	0.39	0.19	0.20	0.17	0.53	24	1.8
Zn _{8.95} K _{1.36} /NaS-N	540	482	0.36	0.20	0.16	0.13	0.27	37	–
Zn _{8.82} K _{1.96} /NaS-N	540	480	0.36	0.20	0.16	0.17	0.33	38	–

^a BET method applied to the N_2 isotherm.^b *t*-Plot method applied to the N_2 isotherm.^c $V_{\text{meso}} = V_{\text{pore}} - V_{\text{micro}}$; in particular, V_{pore} was determined from the amount of N_2 adsorbed at $p/p_0 = 0.99$.^d The amount of acid sites was determined by NH_3 -TPD coupled with mass spectrometry.^e The amount of basic sites was determined by CO_2 -TPD. ^f The amount of carbon deposit was determined by TGA coupled with mass spectrometry, using post-reaction catalysts treated at $T = 550^\circ\text{C}$, $P = 0.1 \text{ MPa}$, $\text{CO}_2:\text{C}_2\text{H}_6:\text{Ar} = 1:1:18$, and $\text{GHSV} = 3600 \text{ mL g}_{\text{cat}}^{-1} \text{ h}^{-1}$.**Fig. 4.** FTIR spectra in the OH region (A), NH_3 -TPD profiles (B, C), and CO_2 -TPD profiles (D, E) of selected micro-sized and nano-sized zeolite catalysts. The color codes indicated in (A) applies also to figures (B)–(E). (For interpretation of the references to colour in this figure, the reader is referred to the web version of this article.)

higher than that of $\text{Zn}_{8.35}/\text{NaS-U}$ (see also the integrated values in Table 1). Although the NH_3 -TPD data show a reduction of the acid strength in the samples upon potassium incorporation, this effect is less evident in the CO_2 -TPD data, likely because of the different response of the NH_3 and CO_2 gas in a TCD detector. However, the intensity of the TCD signal in the K-containing sample is reduced (Fig. 4E).

From the deconvolution and integration of the peaks in the NH_3 -TPD and CO_2 -TPD profiles, it is possible to calculate the amount (and relative ratio) of acid and basic sites (Table 1), which are critical parameters for C_2H_6 activation and CO_2 adsorption [57]. We can observe that adding Zn lowers the acid-to-basic site ratio, while the incorporation of K brings

an increase in this value up to a K loading of 1.36 wt%. Above this content, the relative acid-to-basic site ratio remains constant. From the analysis, we can infer that the micro and nano-sized samples have different (acidic and basic) surface properties. Understanding how these properties are affected by the type of active site is the focus of the following paragraph.

3.3. Oxidation state, metal phase, and Zn dispersion

To study the oxidation state and Zn dispersion in the case of Zn/NaS, we have used a combination of CO-DB-FTIR, UV-Vis-DRS, H_2 -TPR, and

XPS measurements. **Fig. 5A** shows the FTIR spectra of selected micro-sized and nano-sized catalysts after CO adsorption at $-196\text{ }^{\circ}\text{C}$ for 30 min. In fact, CO is a probe molecule that can provide a deeper understanding on the nature of the active sites. The complete deconvolution analysis of the peaks is reported in **Table S2** in the **Supplementary Data**. We observe that CO adsorption on $\text{Zn}_x/\text{SSZ-13}$ results in bands at 2170, 2153, and 2138 cm^{-1} . The band at 2138 cm^{-1} can be attributed to the linear CO adsorption on the surface of ZnO crystals, the band at 2153 cm^{-1} is attributed to symmetric and asymmetric $\text{Zn}^{2+}(\text{CO})_2$ on the surface of ZnO crystals, and the band at 2170 cm^{-1} corresponds to the CO adsorption on isolated (single-site) Zn^{2+} cations entrapped within the zeolite framework [58–61]. The peak at 2162 cm^{-1} is present only on the K-containing sample, and is assigned to CO linearly bonded to alkaline sites, *i.e.* K^+ sites [59–61]. Interestingly, the $\text{Zn}_{1.89}/\text{NaS-U}$ and $\text{Zn}_{8.35}/\text{NaS-U}$ catalysts are characterized by a larger fraction of Zn sites in ZnO clusters (*ca.* 75%) compared to single-site Zn species (*ca.* 25%). Instead, the $\text{Zn}_{1.93}/\text{NaS-N}$ and $\text{Zn}_{8.67}/\text{NaS-N}$ contain a higher fraction of single-site Zn species (*ca.* 70%), compared to the ZnO species (*ca.* 30%). This suggests that the Zn species are better dispersed over nano-sized SSZ-13 than micro-sized SSZ-13 surfaces. This effect is attracting, but is linked with the different surface properties of the micro- and nano-sized zeolites. As shown elsewhere [62], the distribution of a metal on zeolite-type support can vary irrespective of the metal deposition method, namely ion-exchange or incipient wetness impregnation followed by calcination, and can also be directly related to different surface

acidic properties of the individual zeolite crystals, which, as we have shown, indeed vary over micro- and nano-sized samples. Also, the addition of K_2O regulates the status of Zn^{2+} . This analysis can provide further insights into the acidic and basic properties of the materials. In fact, catalysts with a higher fraction of isolated Zn^{2+} ions contain a lower fraction of acidic-to-basic sites and a higher fraction of basic sites (see **Table 1**), in line with the literature [31,46].

The results are confirmed by the UV-Vis-DRS spectra in **Fig. 5B**. All catalysts exhibit an absorption band at *ca.* 265 nm, indicating the formation of single-site Zn^{2+} species [34,63,64]. The intense band at *ca.* 365 nm corresponds to macrocrystal ZnO particles on the external zeolite surface [34,63,64]. Compared to nano-sized NaS-N, the band at 365 nm is stronger for micro-sized NaS-U, suggesting the presence of a high content of macrocrystalline ZnO in NaS-U, in line with the CO-DB-FTIR data.

Fig. 5C presents the H_2 -TPR profiles of $\text{Zn}_x/\text{NaS-U}$, $\text{Zn}_x/\text{NaS-N}$, and $\text{Zn}_x\text{K}_y/\text{NaS-N}$. Previous studies have reported that heterolytic dissociation of H_2 takes place at moderate temperatures (*i.e.*, 100–200 $^{\circ}\text{C}$) when the MFI zeolite contains isolated Zn^{2+} sites [65]. Considering the fact that both nano-sized NaS-N catalysts show higher H_2 consumptions than the micro-sized $\text{Zn}_x/\text{NaS-U}$ between 150 and 350 $^{\circ}\text{C}$ under similar Zn loadings, this further pinpoints that $\text{Zn}_x/\text{NaS-N}$ contain more isolated Zn^{2+} ions, while the Zn species in $\text{Zn}_x/\text{NaS-U}$ are more heterogeneous in nature, and include multinuclear oxygenated clusters [31]. These observations are fully in line with the previous characterizations (**Fig. 5A** and **B**) and are consistent with density functional theory (DFT) calculations based on zeolitic Zn^{2+} cations system [67]. Finally, the reduction peak at *ca.* 450 $^{\circ}\text{C}$ is attributed to the surface Zn oxides which weakly interact with the NaSSZ-13 support. The high-temperature reduction peak around 600 $^{\circ}\text{C}$ is associated with the reduction of binuclear ($\text{Zn-O-Zn})^{2+}$ species as a result of the strong interaction with the framework of zeolite [68]. To sum up, the Zn phase deposits on the SSZ-13 support, forming small ZnO nanoclusters with the $(\text{Zn-O-Zn})^{2+}$ stoichiometry and single-site Zn species in all cases. The relative ratio of these active sites varies over the micro and nano-sized samples since the fraction of single-site species is higher on the nano-sized zeolites, pointing to a better distribution and control of the Zn phase in the latter case (see **Table S2** in the **Supplementary Data** for a quantification).

The Zn 2p core level XPS of $\text{Zn}_{8.35}/\text{NaS-U}$ and $\text{Zn}_{8.82}\text{K}_{1.96}/\text{NaS-N}$ are depicted in **Fig. S5A** and **S5B** in the **Supplementary Data**. The figures show the characteristic Zn 2p doublets corresponding to Zn^{2+} oxidation state [37]. The peaks, centered at the binding energies (BE) of 1023 eV and 1046 eV, correspond to $\text{Zn} 2p_{3/2}$ and $2p_{1/2}$, respectively, with a spin-orbit coupling energy of 23 eV [37]. This indicates the presence of Zn^{2+} (in Zn-O-Zn or single-site form) on both catalysts, which is in line with the new characterization data and previous literature works [36, 37]. The K 2p core level XPS for $\text{Zn}_{8.82}\text{K}_{1.96}/\text{NaS-N}$ is shown in **Fig. S5C** in the **Supplementary Data**. Two peaks, centered at 292 and 293 eV, are present and can be assigned to K^+ , which corroborates the presence of oxidic K_2O (K-O-K) on the surface [66].

3.4. Effect of particle size on the CO_2 -ODHE

Prior to any activity evaluation, a blank test was performed in the absence of any catalyst. As shown in **Fig. S6** in the **Supplementary Data**, C_2H_6 and CO_2 barely react between 550 and 580 $^{\circ}\text{C}$ and, at 650 $^{\circ}\text{C}$, both conversions are still lower than 4%. These observations exclude the potential contribution of gas-phase radical chemistry to drive the reaction [69]. We have also performed the “Madon-Boudart” test, varying the catalyst mesh size of a representative catalyst, and evaluating the materials reactivity in the CO_2 -ODHE. As shown in **Fig. S7**, the conversions of C_2H_6 and CO_2 , and the selectivity to C_2H_4 are constant and independent of the mesh size. Similarly, **Fig. S8** shows the CO_2 -ODHE performance of $\text{Zn}_{8.35}/\text{NaS-U}$ at constant mass-to-flow rate (*W/F*) ratio. With the increase of space velocity, the catalytic activity remains stable. The results, combined with the calculation of the Weisz-Prater criterion

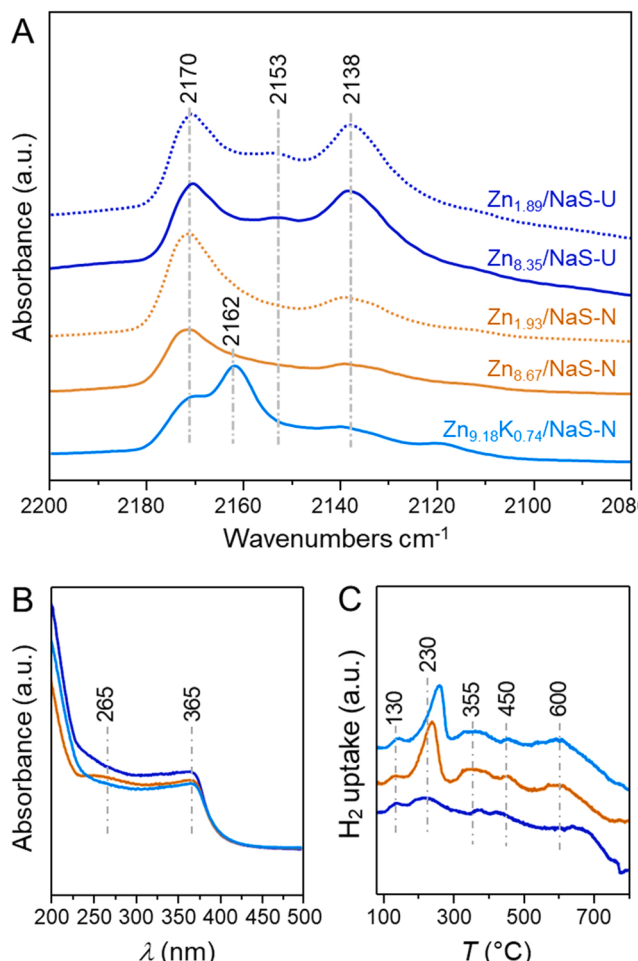


Fig. 5. CO-DB-FTIR (A), UV-Vis-DRS (B), H_2 -TPR (C) profiles of selected Zn modified micro-sized and nano-sized SSZ-13 catalysts. The color codes indicated in (A) applies also to figures (B)–(E). (For interpretation of the references to colour in this figure, the reader is referred to the web version of this article.)

in the [Supplementary Data](#), prove the absence of any internal or external mass transfer limitation. We also excluded any effect given by the Si/Al composition on the catalytic response by preparing and evaluating materials with same Si/Al ratios (Fig. S9 and Table S3).

Fig. 6 shows the performance of a series of NaS-U- and NaS-N-based catalysts in the 550–650 °C temperature range. Additional data are reported in the [Supplementary Data](#) (Table S4). Both parent catalysts, NaS-U and NaS-N, are inactive (Fig. 6A and B). By contrast, the Zn-incorporated catalysts are active, and the conversions of both C₂H₆ and CO₂ increase significantly with the addition of Zn up to a 3 wt% loading, beyond which a plateau is observed. Such Zn-induced enhancement in activity underlines the role of the metal phase in the reaction. At 650 °C, the C₂H₆ and CO₂ conversions over Zn_{8.67}/NaS-N are 66% and 36%, respectively, while over Zn_{8.35}/NaS-U the conversions are 37% and 19%, respectively. In short, under the same reaction conditions, the nano-sized Zn_x/NaS-N is more active than micro-sized Zn_x/NaS-U. In fact, to achieve a C₂H₆ conversion level of *ca.* 40%, Zn_{8.67}/NaS-N requires a temperature of 600 °C, which is 50 °C lower than that for Zn_{8.35}/NaS-U. This effect can be linked with the different distribution of active sites over the samples, and suggests that the isolated Zn²⁺ species are more active. Despite the high activity, all catalysts show a drop in selectivity to C₂H₄, which is more visible over the highly-active Zn_x/NaS-N samples (Fig. 6C). However, it is important to remark at this stage that a fair selectivity (and stability) comparison requires isoconversional conditions (*vide infra*). At 650 °C, the C₂H₄ selectivity decreases in the order of Zn_{1.93}/NaS-N > Zn_{3.25}/NaS-N > Zn_{5.29}/NaS-N > Zn_{8.67}/NaS-N, and the same order is observed over the Zn_x/NaS-U catalysts (Table S4 in the [Supplementary Data](#)). The CO production of Zn_x/NaS-U and Zn_x/NaS-N catalysts at 550 °C and 650 °C is plotted in Fig. 6D. Specifically, the CO formation of Zn_x/NaS-N is markedly higher than that of Zn_x/NaS-U under the same temperature and similar Zn loadings. This might indicate the occurrence of dry reforming above

600 °C, as known from the thermodynamics [70], although the occurrence of the higher Boudouard reaction cannot be excluded. Fig. 6E shows the variation in alkene selectivity as a function of the alkane conversion, signifying that nano-sized zeolite particles are highly active. Fig. 6F presents the Arrhenius plots of Zn_{8.35}/NaS-U and Zn_{8.67}/NaS-N under isoconversional conditions. For the plot, the tests were performed at 550 °C, varying the flow rate to have a C₂H₆ conversion of *ca.* 10% over both catalysts. The two plots are linear, and the estimated apparent activation energy of Zn_{8.67}/NaS-N is 40 kJ mol⁻¹ which is lower than that of Zn_{8.35}/NaS-U (*i.e.*, 52 kJ mol⁻¹). It is important to recognize that these values are in the same order of magnitude of the activation energies reported elsewhere for oxidative and non-oxidative dehydrogenation reactions under similar (mild) temperatures [71,72]. The data in Fig. 6 corroborates that, in comparison to the Zn-loaded micro-sized NaS-U, a higher activity can be obtained using the nano-sized NaS-N, due to the lower activation energy. Given the difference in the type of active sites, we can state that the pivotal role of nano-sized particles in achieving high co-conversions of C₂H₆ and CO₂ is mainly due to the larger presence of isolated Zn sites [73]. This prominent catalytic performance of Zn_x/NaS-N catalysts over that of Zn_x/NaS-U is also highlighted through the correlations between C₂H₆ and CO₂ conversions in Fig. S10 in the [Supplementary Data](#).

A comparison of the activity of our Zn-based sample *vis-à-vis* with previously reported catalysts for CO₂-ODHE is summarized in Table 2. Additional excellent results from the literature are displayed in Table S5. Our Zn_x/NaS-N catalysts show a C₂H₆ conversion and a C₂H₄ yield that are comparable to previously-discovered materials, despite the higher degree of CO₂ conversion over Zn_x/NaS-N. We have also performed comparative studies between O₂-ODHE and CO₂-ODHE over Zn_{8.67}/NaS-N at different conditions, to evaluate the effect of a mild oxidative agent. As depicted in Fig. S11 in the [Supplementary Data](#) and consistently with the literature, the selectivity to ethylene is higher in the case of CO₂-ODHE.

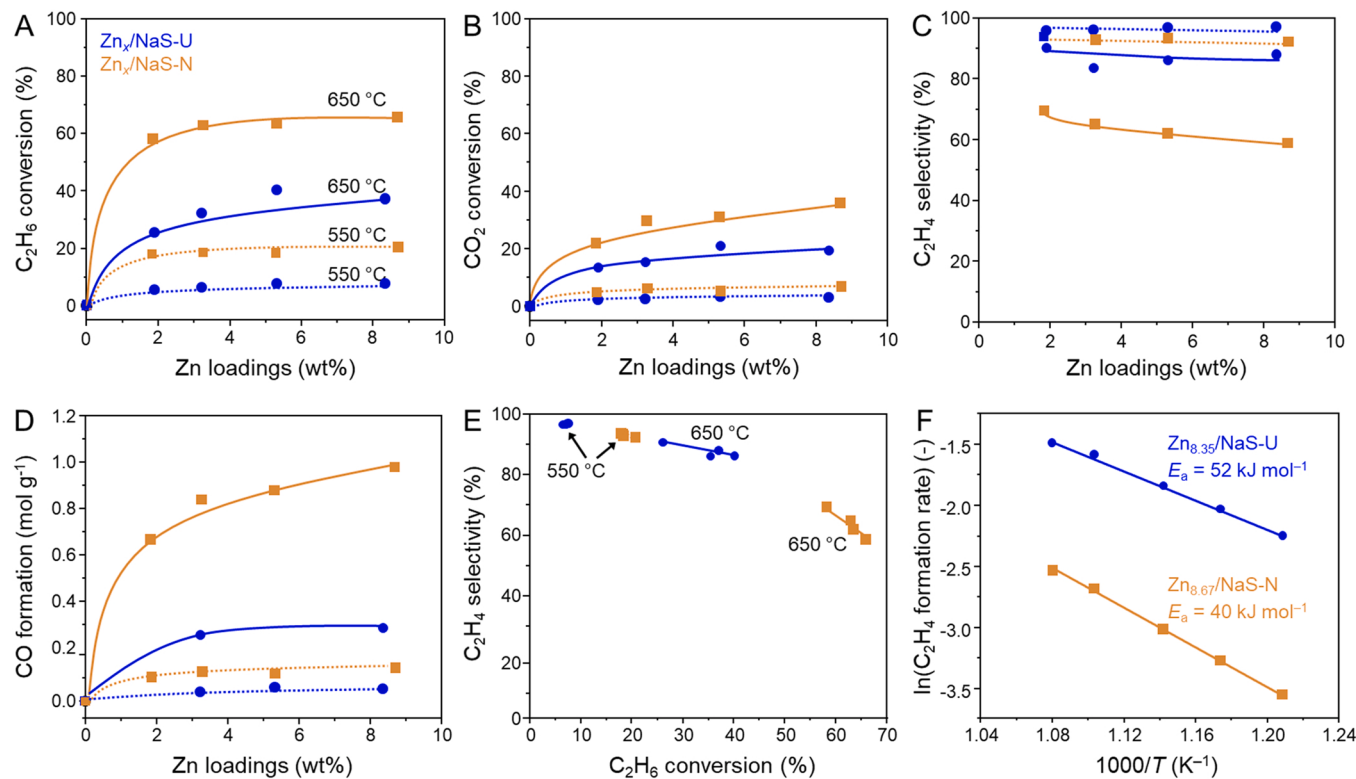


Fig. 6. Effect of Zn content on the CO₂-ODHE performance over micro-sized and nano-sized catalysts (A-D) and correlation between C₂H₄ selectivity and C₂H₆ conversion (E), at $P = 0.1$ MPa, CO₂:C₂H₆:Ar = 1:1:18, and GHSV = 3600 mL g_{cat}⁻¹ h⁻¹. Arrhenius plots for the CO₂-ODHE over Zn_{8.67}/NaS-N and Zn_{8.35}/NaS-U (F) at $T = 550, 580, 600, 630$, and 650 °C, $P = 0.1$ MPa, CO₂:C₂H₆:Ar = 1:1:18, and GHSV = 2400–3600 mL g_{cat}⁻¹ h⁻¹, at a C₂H₆ conversion of *ca.* 10%. Color and sample codes in (A) apply to all figures. (For interpretation of the references to colour in this figure, the reader is referred to the web version of this article.)

Table 2Literature precedents on the catalytic CO_2 -ODHE over various catalytic systems.

Catalyst	mass of catalyst (g)	T ($^{\circ}\text{C}$)	C_2H_6 flow rate (mL min^{-1})	X (C_2H_6) (%)	S (C_2H_4) (%)	Y (C_2H_4) (%)	C_2H_4 formation rate ^a ($\mu\text{mol min}^{-1} \text{g}^{-1}$)	Ref.
CrLi/SO ₄ -SiO ₂	1	650	6.0	17	98	16.7	12.8	[75]
MoVTeNbO	1	650	2.0	49	94	46.1	12.0	[76]
4.8% Cr/HY	1	650	10.0	9	98	8.8	11.3	[77]
Ga-HZSM-5	1	650	10.0	15	94	14.1	18.4	[77]
Cr/H-Beta	1	650	10.0	11	97	10.7	13.9	[77]
5% Cr ₂ O ₃ /SiO ₂	1	650	10.0	56	14	7.8	10.2	[78]
10% Ca-CeO ₂	1	650	10.0	2	92	1.8	2.4	[78]
Ga ₂ O ₃	0.2	650	5.0	6	100	6.0	19.5	[78]
V ₂ O ₅	0.2	650	5.0	6	96	5.8	18.8	[79]
5% Cr/HZSM-5	0.5	650	5.0	11	99	10.9	14.2	[80]
5% Ga ₂ O ₃ /HZSM-5	0.2	650	0.9	9	86	7.7	4.5	[81]
Zn _{8.67} /NaS-N	1	650	3.0	64	62	39.7	15.5	This work
Zn _{9.18} /K _{0.74} /NaS-N	1	650	3.0	57	79	45.0	17.4	This work

^a Although rates should be normalized to the number of active centers and not referred per unit mass of the catalyst, the rate was used here to compare catalysts reported in the literature, and in most of the cases the amount of available active sites at the surface was not reported. For this reason, we have decided to normalize the rate to the catalyst mass.

The advantages of CO_2 as a “soft oxidant” for alkane dehydrogenation have been widely reported in the literature, and include (i) inhibition of deep oxidation of the alkane and improved olefin selectivity, (ii) reduced coke formation, (iii) mitigation of anthropogenic greenhouse gas emissions, and (iv) enhanced equilibrium conversion by removing hydrogen through the reverse water-gas shift (RWGS) reaction [74]. To shed light on the latter aspect, we evaluated the role of the RWGS reaction ($\text{H}_2 + \text{CO}_2 \rightarrow \text{CO} + \text{H}_2\text{O}$) on $\text{Zn}_{8.67}/\text{NaS-N}$ and on bare NaS-N as a benchmark. As shown in Fig. 7A, on $\text{Zn}_{8.67}/\text{NaS-N}$, the CO_2 conversions during RWGS outperform that observed during CO_2 -ODHE, which indicates a partial contribution of RWGS reaction on the formation of CO. To better understand this effect, we have plotted a correlation between the CO formation rate and the CO_2 conversion rate on three representative catalysts (Fig. S12). Given the stoichiometry of the reaction $\text{C}_2\text{H}_6 + \text{CO}_2 \rightarrow \text{C}_2\text{H}_4 + \text{CO} + \text{H}_2\text{O}$, the ratio between CO_2 consumption and the CO formation should be close to the theoretical “1” value. From the plot in Fig. S12, it is visible that the ratio of these three catalysts approaches 1 at low temperatures; however, $\text{Zn}_x/\text{NaS-N}$ and $\text{Zn}_x\text{K}_y/\text{NaS-N}$ exceed this value at high temperatures. This further validates that at lower temperatures, the major contribution of CO formation is likely from the dehydrogenation reaction; with the increase in temperature, both dehydrogenation and RWGS play a role in the formation of CO. From a mechanistic viewpoint, during RWGS, the reaction proceeds through H_2 dissociation on $(\text{Zn}-\text{O}-\text{Zn})^{2+}$ sites, followed by

reaction with CO_2 to form CO, H_2O , and regeneration of the $(\text{Zn}-\text{O}-\text{Zn})^{2+}$ sites (Fig. 7B). During ethane dehydrogenation (Fig. 7C), the heterolytic C_2H_6 dissociation occurs on $(\text{Zn}-\text{O}-\text{Zn})^{2+}$ sites to release C_2H_4 as well as the sites $\text{Zn}^{2+}-\text{H}$ and $\text{Zn}^{2+}-\text{OH}$. In the presence of CO_2 , the reaction continues forming CO and H_2O (Fig. 7C, path 1). In the absence of CO_2 , the associative desorption of H_2 is not kinetically favored because of its high energy barrier. The adsorbed hydrogen species inevitably results in C-C cleavage during ethane dehydrogenation (Fig. 7C path 2) [38,41].

Finally, the C_2H_6 conversion over NaS-U and NaS-N catalysts was evaluated during long-term CO_2 -ODHE, and the first-derivative change is presented in Fig. 8, along with the raw data in Fig. S13 in the *Supplementary Data*. For comparison, the activity of $\text{Zn}_{8.67}/\text{NaS-N}$ and that of $\text{Zn}_{8.35}/\text{NaS-U}$ were compared at isoconversional conditions. Both catalysts deactivate upon time-on-stream (TOS), though the C_2H_6 relative deactivation rate for $\text{Zn}_{8.67}/\text{NaS-N}$ is 2–3% higher than that for $\text{Zn}_{8.35}/\text{NaS-U}$ during the 600 min time on stream.

Overall, despite the significant enhancement in activity over the nano-sized $\text{Zn}_x/\text{NaS-N}$ samples, the occurrence of side reactions seriously affects the selectivity to C_2H_4 at high conversions, leading to a drop in C_2H_4 selectivity to *ca.* 60% at 650°C (Fig. 6). Therefore, restoring a high C_2H_4 selectivity at high conversion and eventually improving the stability are major challenges. For this reason, we have introduced an alkali metal oxide, K_2O , to tune the acid-basic properties of the Zn-SSZ-13 catalysts, and the results will be discussed in the next section.

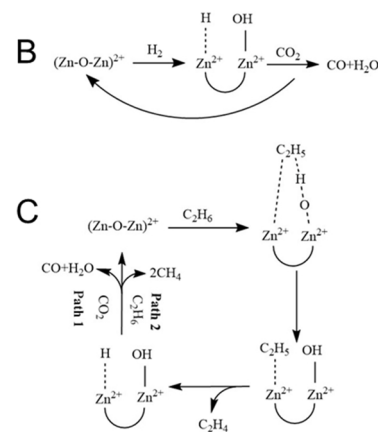
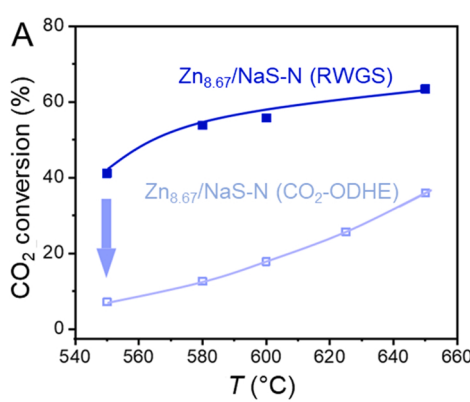


Fig. 7. Activity performance of RWGS on $\text{Zn}_{8.35}/\text{NaS-N}$ and comparison with the CO_2 -ODHE performance of the same catalyst (A) Reaction conditions: $T = 550\text{--}650^{\circ}\text{C}$, $P = 0.1 \text{ MPa}$, $\text{CO}_2:\text{H}_2:\text{Ar} = 1:1:18$ (RWGS), $\text{CO}_2:\text{C}_2\text{H}_6:\text{Ar} = 1:1:18$ (CO_2 -ODHE), GHSV = $3600 \text{ mL g}_{\text{cat}}^{-1} \text{ h}^{-1}$. Proposed reaction paths for the RWGS (B) and for the direct ethane dehydrogenation (DHE), in the presence and absence of CO_2 .

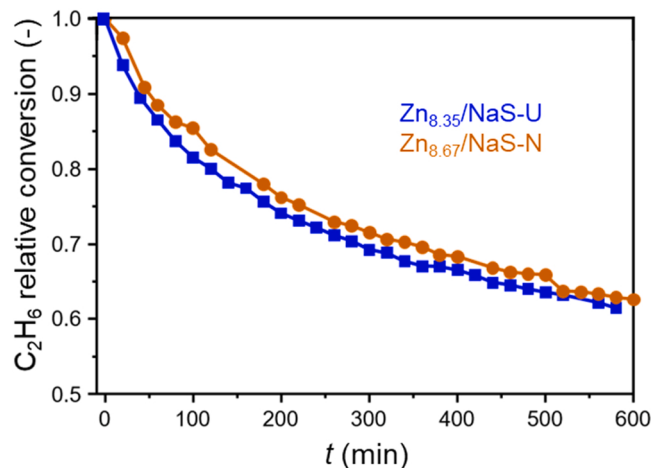


Fig. 8. First derivative changes of C_2H_6 conversion during long-term CO_2 -ODHE over $\text{Zn}_{8.35}/\text{NaS-U}$ and $\text{Zn}_{8.67}/\text{NaS-N}$. Reaction conditions: $T = 550^\circ\text{C}$, $P = 0.1 \text{ MPa}$, $\text{CO}_2:\text{C}_2\text{H}_6:\text{Ar} = 1:1:18$, $\text{GHSV} = 2400\text{--}3600 \text{ mL g}_{\text{cat}}^{-1} \text{ h}^{-1}$, at the same (10%) C_2H_6 conversion.

3.5. Effect of potassium on the catalyst performance

We have prepared a series of $\text{Zn}_x\text{K}_y/\text{NaS-N}$ catalysts with variable K loading and constant Zn content. **Fig. 9** presents the catalytic

performance of the materials, along with the activity of the respective $\text{Zn}_x/\text{NaS-N}$ catalyst as a benchmark. Detailed activity data are given in **Table S4**. In general, adding a minute amount of K (i.e., less than 1.36) results in only a slight reduction in both C_2H_6 and CO_2 conversions. The reduction becomes more pronounced when the K loading is further increased to 1.96. This significant enhancement in selectivity (which can be corroborated also from **Table S6** under similar conversion levels) can be associated with the K-induced modifications on surface acid-base properties. The $\text{Zn}_x\text{K}_y/\text{NaS-N}$ catalysts present lower amounts of acid sites than the $\text{Zn}_x/\text{NaS-N}$ (**Table 1**). Clearly, the addition of K neutralizes the acidity of $\text{Zn}_x/\text{NaS-N}$, thus suppressing the C-C bond cracking to CH_4 while increasing the selectivity toward C_2H_4 . DFT calculations provide evidence to support such statement (*vide infra*). **Fig. S14** in the **Supplementary Data** show the correlation between C_2H_6 and CO_2 conversions on $\text{Zn}_x\text{K}_y/\text{NaS-N}$ catalysts, while **Fig. S15** reports the effect of K loading on the concentration of acid sites and catalytic activity. The results demonstrate that to enhance the C_2H_4 production and achieve higher co-conversions of both reactants, a balance of acid-base properties is of importance. In fact, as shown in **Fig. S15**, the amount of acid sites linearly decreases with the increasing K weight percentage, and the reactant conversions tend to decrease as well. This is indicative of the neutralization of acid sites because of K loading, which leads to the linear loss in activity.

Fig. 10A shows the long-term catalytic performance of $\text{Zn}_{9.18}\text{K}_{0.74}/\text{NaS-N}$ and $\text{Zn}_{8.67}/\text{NaS-N}$ at 650°C . The incorporation of alkali K_2O improves the stability of the catalysts. Coking analysis was performed on the spent catalysts *via* TG-DTG-MS, and the results are shown in **Fig. 10B**

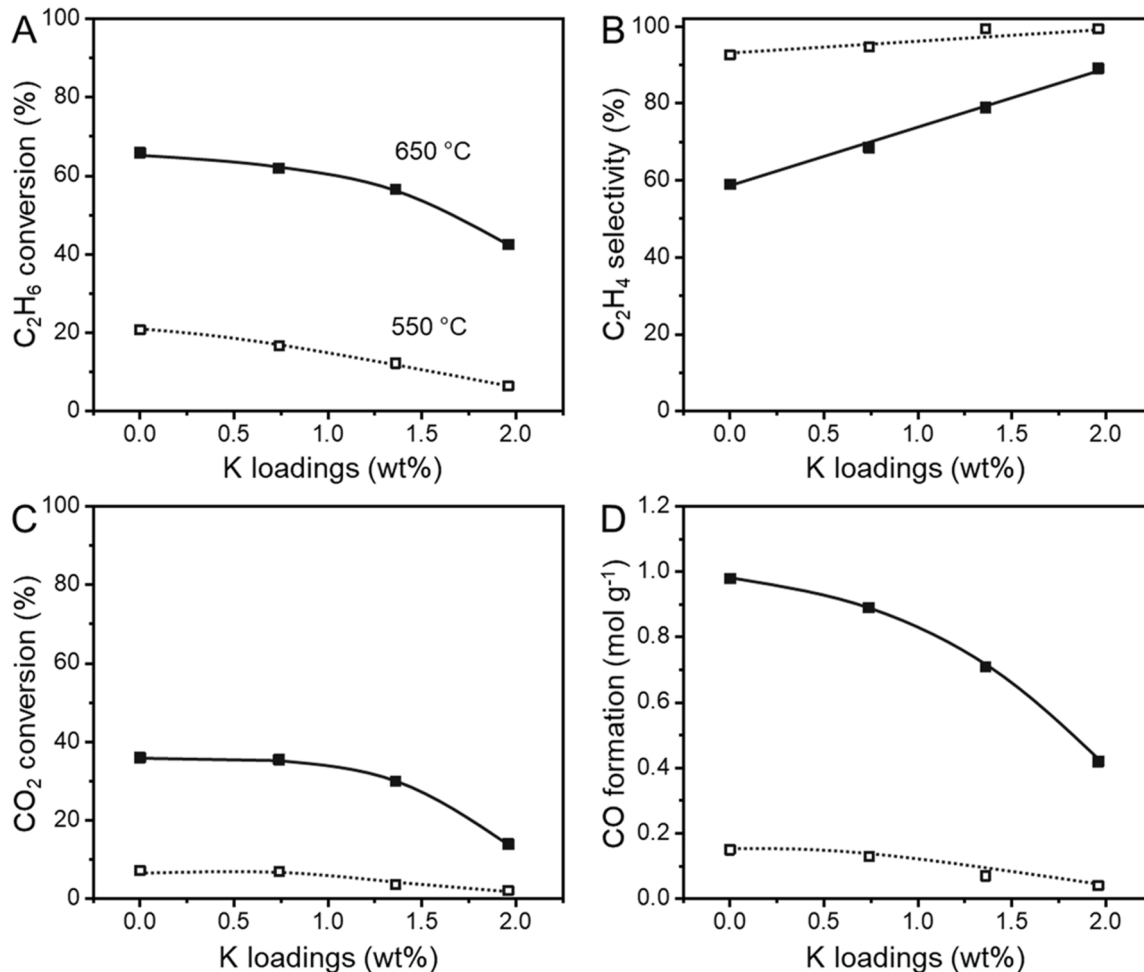


Fig. 9. Effect of K weight percentage on the CO_2 -ODHE performance over selected nano-sized $\text{Zn}_x\text{K}_y/\text{NaS-N}$ ($x = 9.18, 8.95, 8.82$; $y = 0.74, 1.36, 1.96$). The benchmark $\text{Zn}_{8.67}/\text{NaS-N}$ is also displayed for comparison. Reaction conditions: $550\text{--}650^\circ\text{C}$, 0.1 MPa , $\text{CO}_2:\text{C}_2\text{H}_6:\text{Ar} = 1:1:18$, and $\text{GHSV} = 3600 \text{ mL g}_{\text{cat}}^{-1} \text{ h}^{-1}$.

and Table 1. A large amount of coke is generated on $\text{Zn}_{8.67}/\text{NaS-N}$ in comparison with $\text{Zn}_{8.35}/\text{NaS-U}$ due to its higher activity. After the incorporation of K, the coke amount significantly decreases due to the weakened acidity.

DFT calculations have shed light on the promotional effect of K on C_2H_4 selectivity. As shown in Fig. 11 and Fig. 7C, the dehydrogenation mechanisms of C_2H_6 and CO_2 consist of two parts: (i) C_2H_6 activation to desorb C_2H_4 and (ii) the recombination and surface removal of H-containing species. Specifically, after the physical adsorption of C_2H_6 , this molecule is initially dissociated on the active sites through C-H bond cleavage, leading to the formation of ethyl intermediate and a transient Brønsted acid zinc hydroxyl group ($\text{Zn}^{2+}\text{-OH}$) [40]. Then, the ethyl intermediate would undergo a second C-H bond cleavage to form and release C_2H_4 , leaving another $\text{Zn}^{2+}\text{-H}$ site on the surface of catalyst.

As proposed in the literature, the rate determining step for the dehydrogenation of light alkanes is the recombination and removal of the remaining H-adsorbed species to give CO and H_2O [38,41]. As shown from Fig. 11, the presence of CO_2 facilitates the removal of adsorbates by forming HCOOH species on both (Zn-O-Zn) $^{2+}$ and K_2O -neighbored (Zn-O-Zn) $^{2+}$. In particular, the activation energy barrier of this step is lowered in comparison to the direct H_2 removal through desorption from direct ethane dehydrogenation [37]. At the same time, the rate determining step shifts to the second C-H bond dissociation (TS2) to desorb C_2H_4 . Compared with (Zn-O-Zn) $^{2+}$, adding K reduces very slightly this energy barrier, but does not alter the remaining energy profile. In fact, the medium strong acid of ZnOH becomes weak due to the influence of K_2O , therefore resulting in the charge transfer to the oxygen of ZnOH and in the suppression on proton transfer. The ZnOH -induced side reaction, hydrogenolysis, would result in the generation of CH_4 (see Fig. 7B and C). K_2O -neighbored ZnOH significantly reduces the concentration of acid sites, therefore the hydrogenolysis to CH_4 is inhibited. This is consistent with our experimental results, in which the CH_4 selectivity over $\text{Zn}_{8.82}\text{K}_{1.96}/\text{NaS-N}$ is remarkably reduced in comparison to the K-free counterpart (Table S4 in the Supplementary Data).

4. Conclusions

K-modified Zn on micro- and nano-sized SSZ-13 were prepared, and their catalytic performance was evaluated in CO_2 -ODHE reaction. The Zn-modified nano-sized SSZ-13 catalysts, namely $\text{Zn}_x/\text{NaS-N}$, are more

active in the conversion of CO_2 and C_2H_6 in comparison to the micro-sized counterparts, namely $\text{Zn}_x/\text{NaS-U}$, indicating the critical role of small crystallite sizes in improving the activity through the increased presence of isolated Zn sites. The increased addition of Zn results in the enhancement in conversions, but is accompanied with the drop in C_2H_4 selectivity. Adding K enables the preservation of the high C_2H_4 selectivity and significantly improves the stability. Optimal activity and selectivity are achieved over $\text{Zn}_{9.18}\text{K}_{0.74}/\text{NaS-N}$, on which the C_2H_6 conversion, CO_2 conversion, and C_2H_4 selectivity at 650 °C are 60.3, 52.9, and 73.4, respectively. Characterization results demonstrate that acid sites that are responsible for heterolytic C_2H_6 dissociation to C_2H_4 are (Zn-O-Zn) $^{2+}$. However, the Brønsted acid ZnOH with medium-strong acidity, generated during the transient process of C_2H_6 dehydrogenation, can facilitate the C-C cleavage to form CH_4 through hydrogenolysis, leading to lower C_2H_4 selectivity but higher CH_4 selectivity. The presence of K_2O enables the charge transfer to the oxygen of ZnOH and thus the suppression proton transfer, forming weak acid sites. As a result, the hydrogenolysis is substantially suppressed, leading to well-retained C_2H_4 selectivity and improved stability. In the direct C_2H_6 dehydrogenation, the associative desorption of hydrogen is proposed as the RDS. DFT calculations demonstrate that both (Zn-O-Zn) $^{2+}$ and K_2O -neighbored (Zn-O-Zn) $^{2+}$ sites can promote this step by lowering the activation barrier of surface hydrogen removal by reacting with CO_2 . Our results not only provide evidence to achieve better performance in activating both C_2H_6 and CO_2 molecules, but also shed light on the importance of tuning the surface acid-base properties in manipulating activity and selectivity for CO_2 -assisted dehydrogenation of light alkanes.

CRediT authorship contribution statement

Zhenmei Zhang and Yulin Jiang prepared the catalysts and run the catalytic testing in CO_2 -ODHE. Ning He performed the DFT calculations. Siyang Yan conducted microscopy characterizations. Peng Guo performed the XPS characterizations and TPD/TPR studies. Zhenmei Zhang, Guang Xiong, and Ji Su made spectroscopy characterizations. Gianvito Vilé, Xiao Jiang, and Jiaxu Liu conceived the work, coordinated the study, analyzed and interpreted the data. Gianvito Vilé, Xiao Jiang, and Jiaxu Liu wrote the manuscript. The manuscript (in the original and revised form) was finally read and approved by all co-authors.

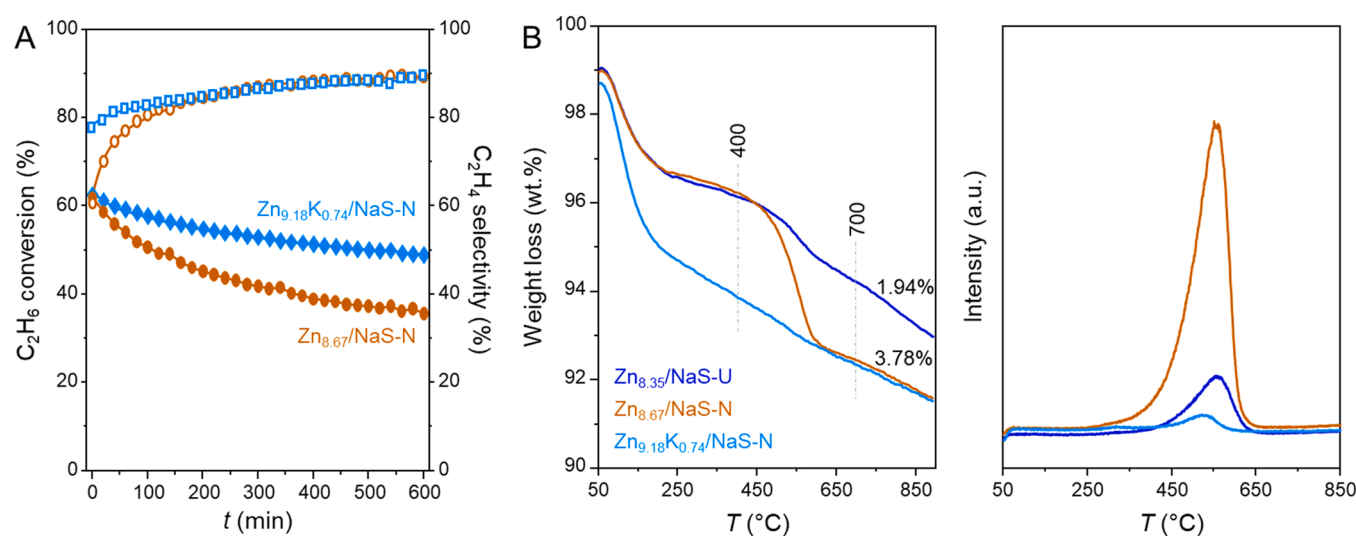


Fig. 10. Long-term stability (A) of $\text{Zn}_{9.18}\text{K}_{0.74}/\text{NaS-N}$ and $\text{Zn}_{8.67}/\text{NaS-N}$ for CO_2 -ODHE test. Reaction conditions: $T = 650$ °C, $P = 0.1$ MPa, $\text{CO}_2:\text{C}_2\text{H}_6:\text{Ar} = 1:1:18$, GHSV = 3600 $\text{mL g}_{\text{cat}}^{-1} \text{h}^{-1}$. TG-DTG results and CO_2 -MS evolution (B) over selected micro-sized and nano-sized SSZ-13 catalysts (B).

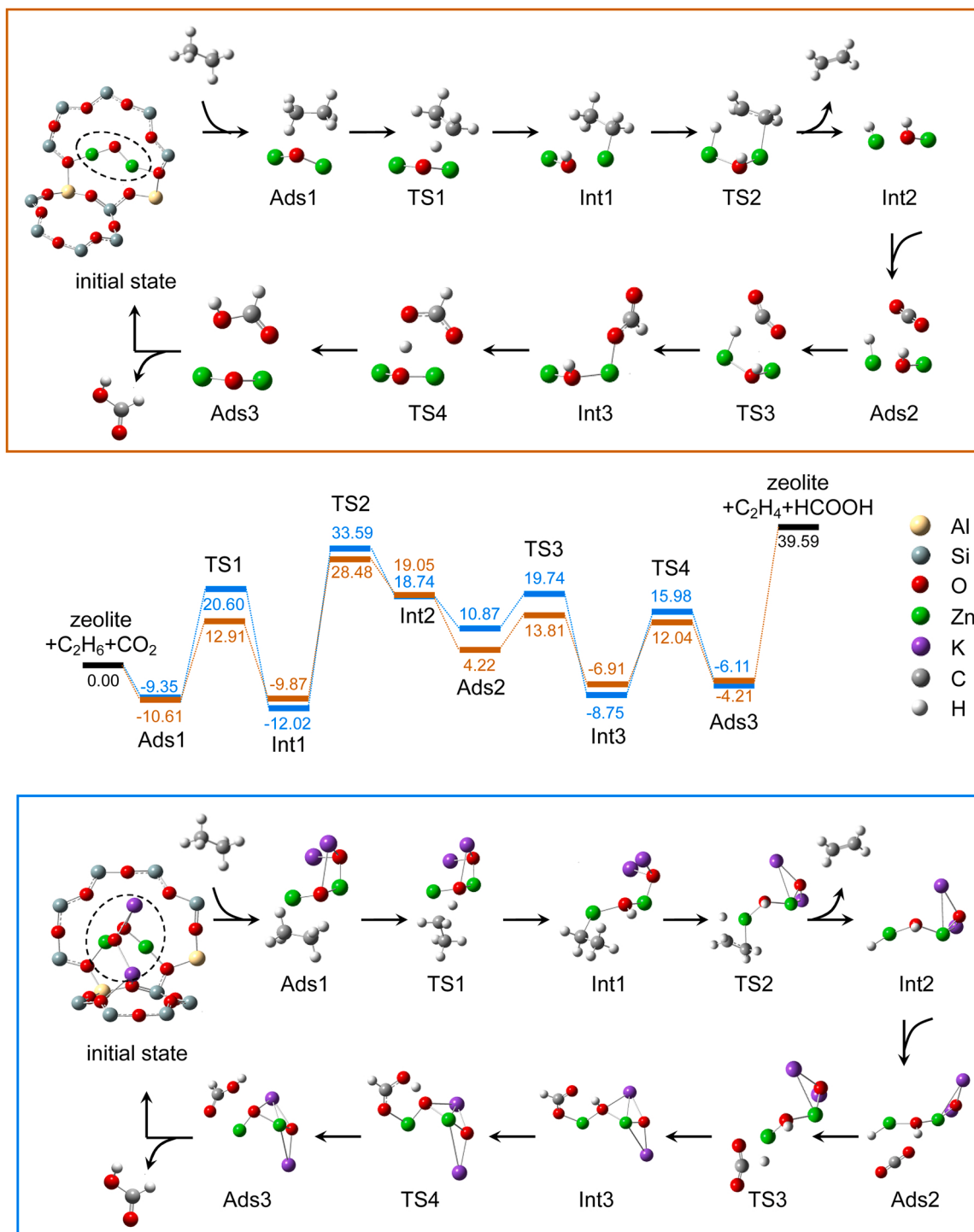


Fig. 11. Energy profiles for the CO₂-ODHE on the modeled (Zn-O-Zn)²⁺ surface (profile and inset in orange), and over the K-modified (Zn-O-Zn)²⁺ surface (profile and inset in blue). (For interpretation of the references to colour in this figure, the reader is referred to the web version of this article.)

Declaration of Competing Interest

The authors declare that they have no known competing financial interests or personal relationships that could have appeared to influence the work reported in this paper.

Acknowledgements

J.L. acknowledges the financial support from the Fundamental Research Funds for the Central Universities (DUT20LAB127) and Dalian

High-level Talent Innovation Support Program (2017RQ011). G.V. thanks Politecnico di Milano for starting up funding.

Appendix A. Supporting information

Supplementary data associated with this article can be found in the online version at doi:10.1016/j.apcatb.2021.120947.

References

- [1] Z. Xie, Y. Xu, M. Xie, X. Chen, J.H. Lee, E. Stavitski, S. Kattel, J.G. Chen, Reactions of CO₂ and ethane enable CO bond insertion for production of C₃ oxygenates, *Nat. Commun.* 11 (2020) 1887.
- [2] M.A. Atanga, F. Rezaei, A. Jawad, M. Fitch, A.A. Rownaghi, Oxidative dehydrogenation of propane to propylene with carbon dioxide, *Appl. Catal. B* 220 (2018) 429–445.
- [3] E. Gomez, B. Yan, S. Kattel, J.G. Chen, Carbon dioxide reduction in tandem with light-alkane dehydrogenation, *Nat. Rev. Chem.* 3 (2019) 638–649.
- [4] J.J. Sattler, J. Ruiz-Martinez, E. Santillan-Jimenez, B.M. Weckhuysen, Catalytic dehydrogenation of light alkanes on metals and metal oxides, *Chem. Rev.* 114 (2014) 10613–10653.
- [5] B. Chu, H. An, T.A. Nijhuis, J.C. Schouten, Y. Cheng, A self-redox pure-phase M₁ MoVNbTeO/CeO₂ nanocomposite as a highly active catalyst for oxidative dehydrogenation of ethane, *J. Catal.* 329 (2015) 471–478.
- [6] E.V. Kondratenko, M. Cherian, M. Baerns, D.S. Su, R. Schlogl, X. Wang, I.E. Wachs, Oxidative dehydrogenation of propane over V/MCM-41 catalysts: comparison of O₂ and N₂O as oxidants, *J. Catal.* 234 (2005) 131–142.
- [7] S. Sugiyama, T. Osaka, Y. Hirata, K.-I. Sotowa, Enhancement of the activity for oxidative dehydrogenation of propane on calcium hydroxyapatite substituted with vanadate, *Appl. Catal. A* 312 (2006) 52–58.
- [8] P. Deshlakra, E. Iglesia, Reactivity and selectivity descriptors for the activation of C–H bonds in hydrocarbons and oxygenates on metal oxides, *J. Phys. Chem. C* 120 (2016) 16741–16760.
- [9] M. Myint, B. Yan, J. Wan, S. Zhao, J.G. Chen, Reforming and oxidative dehydrogenation of ethane with CO₂ as a soft oxidant over bimetallic catalysts, *J. Catal.* 343 (2016) 168–177.
- [10] R. Bulanek, B. Wichterlova, K. Novoveska, V. Kreibich, Oxidation of propane with oxygen and/or nitrous oxide over Fe-ZSM-5 with low iron concentrations, *Appl. Catal. A* 264 (2004) 13–22.
- [11] C.R. Adams, T.J. Jennings, Catalytic oxidations with sulfur dioxide: II. Alkylaromatics, *J. Catal.* 17 (1970) 157–177.
- [12] A.L. Sun, Z.F. Qin, J.G. Wang, Reaction coupling of ethylbenzene dehydrogenation with water-gas shift, *Appl. Catal. A* 234 (2002) 179–189.
- [13] G. Centi, S. Perathoner, Heterogeneous catalytic reactions with CO₂: Status and perspectives, in: S.E. Park, J.S. Chang, K.W. Lee (Eds.) *Carbon Dioxide Utilization for Global Sustainability*, 2004, pp. 1–8.
- [14] Z.-Z. Yang, L.-N. He, J. Gao, A.-H. Liu, B. Yu, Carbon dioxide utilization with C–N bond formation: carbon dioxide capture and subsequent conversion, *Energy Environ. Sci.* 5 (2012) 6602–6639.
- [15] X. Jiang, X. Nie, X. Guo, C. Song, J.G. Chen, Recent advances in carbon dioxide hydrogenation to methanol via heterogeneous catalysis, *Chem. Rev.* 120 (2020) 7984–8034.
- [16] T. Sakakura, J.-C. Choi, H. Yasuda, Transformation of carbon dioxide, *Chem. Rev.* 107 (2007) 2365–2387.
- [17] S.A. Theofanidis, C. Loizidis, E. Heracleous, A.A. Lemonidou, CO₂-oxidative ethane dehydrogenation over highly efficient carbon-resistant Fe-catalysts, *J. Catal.* 388 (2020) 52–65.
- [18] Y. Cheng, C. Miao, W. Hua, Y. Yue, Z. Gao, Cr/ZSM-5 for ethane dehydrogenation: enhanced catalytic activity through surface silanol, *Appl. Catal. A* 532 (2017) 111–119.
- [19] S. Wang, K. Murata, T. Hayakawa, S. Hamakawa, K. Suzuki, Dehydrogenation of ethane with carbon dioxide over supported chromium oxide catalysts, *Appl. Catal. A* 196 (2000) 1–8.
- [20] F. Zhang, R. Wu, Y. Yue, W. Yang, S. Gu, C. Miao, W. Hua, Z. Gao, Chromium oxide supported on ZSM-5 as a novel efficient catalyst for dehydrogenation of propane with CO₂, *Micro Mesopor. Mat.* 145 (2011) 194–199.
- [21] K. Nakagawa, C. Kajita, K. Okumura, N. Ikenaga, M. Nishitani-Gamo, T. Ando, T. Kobayashi, T. Suzuki, Role of carbon dioxide in the dehydrogenation of ethane over gallium-loaded catalysts, *J. Catal.* 203 (2001) 87–93.
- [22] N. Mimura, M. Okamoto, H. Yamashita, S.T. Oyama, K. Murata, Oxidative dehydrogenation of ethane over Cr/ZSM-5 catalysts using CO₂ as an oxidant, *J. Phys. Chem. B* 110 (2006) 21764–21770.
- [23] X. Lin, C.A. Hoel, W.M.H. Sachtle, K.R. Poepelmeier, E. Weitz, Oxidative dehydrogenation (ODH) of ethane with O₂ as oxidant on selected transition metal-loaded zeolites, *J. Catal.* 265 (2009) 54–62.
- [24] A. Toth, G. Halasi, F. Solyomosi, Reactions of ethane with CO₂ over supported Au, *J. Catal.* 330 (2015) 1–5.
- [25] X. Zhao, X. Wang, Oxidative dehydrogenation of ethane to ethylene by carbon dioxide over Cr/TS-1 catalysts, *Catal. Commun.* 7 (2006) 633–638.
- [26] X. Shi, S. Ji, K. Wang, C. Li, Oxidative Dehydrogenation of Ethane with CO₂ over Novel Cr/SBA-15/Al₂O₃/FeCrAl Monolithic Catalysts, *Energy Fuels* 22 (2008) 3631–3638.
- [27] S. Teketel, W. Skistad, S. Benard, U. Olsbye, K.P. Lillerud, P. Beato, S. Svelle, Shape selectivity in the conversion of methanol to hydrocarbons: the catalytic performance of one-dimensional 10-ring zeolites: ZSM-22, ZSM-23, ZSM-48, and EU-1, *ACS Catal.* 2 (2011) 26–37.
- [28] A. Corma, Inorganic solid acids and their use in acid-catalyzed hydrocarbon reactions, *Chem. Rev.* 95 (1995) 559–614.
- [29] Z. Chen, Z.-M. Cui, P. Li, C.-Y. Cao, Y.-L. Hong, Z.-y Wu, W.-G. Song, Diffusion induced reactant shape selectivity inside mesoporous pores of pd@meso-sio² nanoreactor in suzuki coupling reactions, *J. Phys. Chem. C* 116 (2012) 14986–14991.
- [30] K. Beschmann, L. Riekert, U. Muller, Shape-selectivity of large and small crystals of zeolite ZSM-5, *J. Catal.* 145 (1994) 243–245.
- [31] S.M.T. Almutairi, B. Mezari, P.C.M.M. Magusin, E.A. Pidko, E.J.M. Hensen, Structure and reactivity of Zn-modified ZSM-5 zeolites: the importance of clustered cationic Zn complexes, *ACS Catal.* 2 (2011) 71–83.
- [32] A.A. Gabrienko, S.S. Arzumanov, A.V. Toktarev, I.G. Danilova, I.P. Prosvirin, V. V. Kriventsov, V.I. Zaikovskii, D. Freude, A.G. Stepanov, Different efficiency of Zn²⁺ and ZnO species for methane activation on Zn-modified zeolite, *ACS Catal.* 7 (2017) 1818–1830.
- [33] N.M. Schweitzer, B. Hu, U. Das, H. Kim, J. Greeley, L.A. Curtiss, P.C. Stair, J. T. Miller, A.S. Hock, Propylene hydrogenation and propane dehydrogenation by a single-site Zn²⁺ on silica catalyst, *ACS Catal.* 4 (2014) 1091–1098.
- [34] A. Mehdad, R.F. Lobo, Ethane and ethylene aromatization on zinc-containing zeolites, *Catal. Sci. Technol.* 7 (2017) 3562–3572.
- [35] P. Zhang, X. Yang, X. Hou, J. Mi, Z. Yuan, J. Huang, C. Stampfl, Active sites and mechanism of the direct conversion of methane and carbon dioxide to acetic acid over the zinc-modified H-ZSM-5 zeolite, *Catal. Sci. Technol.* 9 (2019) 6297–6307.
- [36] M.A. Shah, S. Raynes, D.C. Apperley, R.A. Taylor, Framework effects on activation and functionalisation of methane in zinc-exchanged zeolites, *ChemPhysChem* 21 (2020) 673–679.
- [37] J. Liu, N. He, Z. Zhang, J. Yang, X. Jiang, Z. Zhang, J. Su, M. Shu, R. Si, G. Xiong, H. B.-Xie, G. Vilé, Highly-dispersed zinc species on zeolites for the continuous and selective dehydrogenation of ethane with CO₂ as a soft oxidant, *ACS Catal.* 11 (2021) 2819–2830.
- [38] J. Liu, N. He, W. Zhou, L. Lin, G. Liu, C. Liu, J. Wang, Q. Xin, G. Xiong, H. Guo, Isobutane aromatization over a complete Lewis acid Zn/HZSM-5 zeolite catalyst: performance and mechanism, *Catal. Sci. Technol.* 8 (2018) 4018–4029.
- [39] J. Liu, N. He, W. Zhou, M. Shu, L. Lin, J. Wang, R. Si, G. Xiong, Q. Xin, H. Guo, Operando dual beam FTIR spectroscopy unravels the promotional effect of Zn on HZSM-5 in iso-butane aromatization, *Catal. Sci. Technol.* 9 (2019) 1609–1620.
- [40] J. Liu, L. Lin, J. Wang, W. Zhou, C. Miao, C. Liu, N. He, Q. Xin, H. Guo, Transient Brønsted acid sites in propene aromatization over Zn-modified HZSM-5 detected by operando dual-beam FTIR, *J. Phys. Chem. C* 123 (2019) 7283–7289.
- [41] J. Liu, N. He, Y. Zhao, L. Lin, W. Zhou, G. Xiong, H. Xie, H. Guo, The crucial role of skeleton structure and carbon number on short-chain alkane activation over Zn/HZSM-5 catalyst: an experimental and computational study, *Catal. Lett.* 148 (2018) 2069–2081.
- [42] A. Tóth, G. Halasi, F. Solyomosi, Reactions of ethane with CO₂ over supported Au, *J. Catal.* 330 (2015) 1–5.
- [43] M.J. Frisch, G.W. Trucks, H.B. Schlegel, G.E. Scuseria, M.A. Robb, J.R. Cheeseman, G. Scalmani, V. Barone, B. Mennucci, G.A. Petersson, H. Nakatsuji, Gaussian 09, revision A.1. Gaussian, Inc.: Wallingford, CT, 2009.
- [44] V.P. Ananikov, D.G. Musaev, K. Morokuma, Real size of ligands, reactants and catalysts: studies of structure, reactivity and selectivity by ONIOM and other hybrid computational approaches, *J. Mol. Catal. A* 324 (2010) 104–119.
- [45] J.-D. Chai, M. Head-Gordon, Long-range corrected hybrid density functionals with damped atom–atom dispersion corrections, *Phys. Chem. Chem. Phys.* 10 (2008) 6615–6620.
- [46] E.A. Pidko, R.A. van Santen, Activation of light alkanes over zinc species stabilized in ZSM-5 zeolite: a comprehensive DFT study, *J. Phys. Chem. C* 111 (2007) 2643–2655.
- [47] J. Wang, L. Shao, C. Wang, J. Wang, M. Shen, W. Li, Controllable preparation of various crystal size and nature of intra-crystalline diffusion in Cu/SSZ-13 NH₃-SCR catalysts, *J. Catal.* 367 (2018) 221–228.
- [48] J. Wang, Z. Peng, Y. Chen, W. Bao, L. Chang, G. Feng, In-situ hydrothermal synthesis of Cu-SSZ-13/cordierite for the catalytic removal of NO_x from diesel vehicles by NH₃, *Chem. Eng. J.* 263 (2015) 9–19.
- [49] Z. Li, M.T. Navarro, J. Martínez-Triguero, J. Yu, A. Corma, Synthesis of nano-SSZ-13 and its application in the reaction of methanol to olefins, *Catal. Sci. Technol.* 6 (2016) 5856–5863.
- [50] X. Zhu, J.P. Hofmann, B. Mezari, N. Kosinov, L. Wu, Q. Qian, B.M. Weckhuysen, S. Asahina, J. Ruiz-Martínez, E.J.M. Hensen, Trimodal porous hierarchical SSZ-13 Zeolite with improved catalytic performance in the methanol-to-olefins reaction, *ACS Catal.* 6 (2016) 2163–2177.
- [51] K. Barbera, F. Bonino, S. Bordiga, T.V.W. Janssens, P. Beato, Structure–deactivation relationship for ZSM-5 catalysts governed by framework defects, *J. Catal.* 280 (2011) 196–205.
- [52] T.I. Kyriani, F. Moreau, V.V. Rozanova, E.A. Rozanova, Identification of SH groups in zeolite-supported HDS catalysts by FTIR spectroscopy, *J. Mol. Struct.* 410 (1997) 103–110.
- [53] Y. Cheng, T. Lei, C. Miao, W. Hua, Y. Yue, Z. Gao, Ga₂O₃/NaZSM-5 for C₂H₆ dehydrogenation in the presence of CO₂: Conjugated effect of silanol, *Micro Mesopor. Mat.* 268 (2018) 235–242.
- [54] L. Wang, W. Li, S.J. Schmiege, D. Weng, Role of Brønsted acidity in NH₃ selective catalytic reduction reaction on Cu/SAPO-34 catalysts, *J. Catal.* 324 (2015) 98–106.
- [55] F. Gao, Y. Wang, N.M. Washton, M. Kollár, J. Szanyi, C.H.F. Peden, Effects of alkali and alkaline earth cations on the activity and hydrothermal stability of Cu/SSZ-13 NH₃-SCR catalysts, *ACS Catal.* 5 (2015) 6780–6791.
- [56] T. Zhang, J. Li, J. Liu, D. Wang, Z. Zhao, K. Cheng, J. Li, High activity and wide temperature window of Fe–Cu–SSZ-13 in the selective catalytic reduction of NO with ammonia, *AIChE J.* 61 (2015) 3825–3837.
- [57] S. Deng, H. Li, S. Li, Y. Zhang, Activity and characterization of modified Cr₂O₃/ZrO₂ nano-composite catalysts for oxidative dehydrogenation of ethane to ethylene with CO₂, *J. Mol. Catal. A* 268 (2007) 169–175.
- [58] G.L. Griffin, J.T. Yates, Coadsorption studies of CO and H₂ on ZnO, *J. Chem. Phys.* 77 (1982) 3751–3758.

[59] Y. Kolyagin, V. Ordovsky, Y. Khimyak, A. Rebrov, F. Fajula, I. Ivanova, Initial stages of propane activation over Zn/MFI catalyst studied by in situ NMR and IR spectroscopic techniques, *J. Catal.* 238 (2006) 122–133.

[60] M. Andersen, X. Yu, M. Kick, Y. Wang, C. Wöll, K. Reuter, Infrared reflection-absorption spectroscopy and density functional theory investigations of ultrathin ZnO films formed on Ag(111), *J. Phys. Chem. C* 122 (2018) 4963–4971.

[61] R. Kefirov, A. Penkova, K. Hadjiivanov, S. Dzwigaj, M. Che, Stabilization of Cu⁺ ions in BEA zeolite: study by FTIR spectroscopy of adsorbed CO and TPR, *Micro Mesopor. Mat.* 116 (2008) 180–187.

[62] L.I. van der Wal, K.P. de Jong, J. Zečević, The origin of metal loading heterogeneities in Pt/Zeolite Y bifunctional catalysts, *ChemCatChem* 11 (2019) 4081–4088.

[63] Y.G. Kolyagin, V.V. Ordovsky, Y.Z. Khimyak, A.I. Rebrov, F. Fajula, I.I. Ivanova, Initial stages of propane activation over Zn/MFI catalyst studied by in situ NMR and IR spectroscopic techniques, *J. Catal.* 238 (2006) 122–133.

[64] J. Chen, Z.C. Feng, P.L. Ying, C. Li, ZnO clusters encapsulated inside micropores of zeolites studied by UV Raman and laser-induced luminescence spectroscopies, *J. Phys. Chem. B* 108 (2004) 12669–12676.

[65] V.B. Kazansky, A.I. Serykh, Unusual localization of zinc cations in MFI zeolites modified by different ways of preparation, *Phys. Chem. Chem. Phys.* 6 (2004) 3760–3764.

[66] X. Shi, S. Ji, K. Wang, Oxidative dehydrogenation of ethane to ethylene with carbon dioxide over Cr-Ce/SBA-15 Catalysts, *Catal. Lett.* 125 (2008) 331–339.

[67] L.A.M.M. Barbosa, R.A. van Santen, The activation of H₂ by zeolitic Zn(II) cations, *J. Phys. Chem. C* 111 (2007) 8337–8348.

[68] C. Song, X. Li, X. Zhu, S. Liu, F. Chen, F. Liu, L. Xu, Influence of the state of Zn species over Zn-ZSM-5/ZSM-11 on the coupling effects of cofeeding n-butane with methanol, *Appl. Catal. A* 519 (2016) 48–55.

[69] J.M. Venegas, L. Hermans, The influence of reactor parameters on the boron nitride-catalyzed oxidative dehydrogenation of propane, *Org. Process Res. Dev.* 22 (2018) 1644–1652.

[70] M.D. Porosoff, M.N.Z. Myint, S. Kattel, Z. Xie, E. Gomez, P. Liu, J.G. Chen, Identifying different types of catalysts for CO₂ reduction by ethane through dry reforming and oxidative dehydrogenation, *Angew. Chem. Int. Ed.* 54 (2015) 15501–15505.

[71] V. Balcaen, I. Sack, M. Olea, G.B. Marin, Transient kinetic modeling of the oxidative dehydrogenation of propane over a vanadia-based catalyst in the absence of O₂, *Appl. Catal. A* 371 (2009) 31–42.

[72] J. Shan, N. Janvelyan, H. Li, J. Liu, T.M. Egle, J. Ye, M.M. Biener, J. Biener, C. M. Friend, M. Flytzani-Stephanopoulos, Selective non-oxidative dehydrogenation of ethanol to acetaldehyde and hydrogen on highly dilute NiCu alloys, *Appl. Catal. B* 205 (2005) 541–550.

[73] A.H. Motagamwala, R. Almallahi, J. Wortman, V. Omoze Igenegbai, S. Linic, Stable and selective catalysts for propane dehydrogenation operating at thermodynamic limit, *Science* 373 (2021) 217–222.

[74] M. Chen, J.-L. Wu, Y.-M. Liu, Y. Cao, L. Guo, H.-Y. He, K.-N. Fan, Study in support effect of In₂O₃/MO_x (M = Al, Si, Zr) catalysts for dehydrogenation of propane in the presence of CO₂, *Appl. Catal. A-Gen.* 407 (2011) 20–28.

[75] S.B. Wang, K. Murata, T. Hayakawa, S. Hamakawa, K. Suzuki, Effect of promoters on catalytic performance of Cr/SiO₂ catalysts in oxidative dehydrogenation of ethane with carbon dioxide, *Catal. Lett.* 73 (2001) 107–111.

[76] J.M. López Nieto, P. Botella, M.I. Vázquez, A. Dejoz, The selective oxidative dehydrogenation of ethane over hydrothermally synthesised MoVTeNb catalysts, *Chem. Commun.* (2002) 1906–1907.

[77] N. Mimura, I. Takahara, M. Inaba, M. Okamoto, K. Murata, High-performance Cr/H-ZSM-5 catalysts for oxidative dehydrogenation of ethane to ethylene with CO₂ as an oxidant, *Catal. Commun.* 3 (2002) 257–262.

[78] R.X. Valenzuela, G. Bueno, V. Cortés Corberán, Y. Xu, C. Chen, Selective oxidative dehydrogenation of ethane with CO₂ over CeO₂-based catalysts, *Catal. Today* 61 (2000) 43–48.

[79] K. Nakagawa, C. Kajita, N. Ikenaga, T. Suzuki, T. Kobayashi, M. Nishitani-Gamo, T. Ando, The role of chemisorbed oxygen on diamond surfaces for the dehydrogenation of ethane in the presence of carbon dioxide, *J. Phys. Chem. B* 107 (2003) 4048–4056.

[80] F. Rahmani, M. Haghghi, M. Amini, The beneficial utilization of natural zeolite in preparation of Cr/clinoptilolite nanocatalyst used in CO₂-oxidative dehydrogenation of ethane to ethylene, *J. Ind. Eng. Chem.* 31 (2015) 142–155.

[81] Z. Shen, J. Liu, H. Xu, Y. Yue, W. Hua, W. Shen, Dehydrogenation of ethane to ethylene over a highly efficient Ga₂O₃/HZSM-5 catalyst in the presence of CO₂, *Appl. Catal. A* 356 (2009) 148–153.